Design and Characterization of Optical Metasurface Systems

Elyas Bayati

A dissertation

submitted in partial fulfillment of the

requirements for the degree of

Doctor of Philosophy

University of Washington

2022

Reading Committee:

Prof. Arka Majumdar, Chair

Prof. Karl F. Böhringer

Prof. Joshua R. Smith

Program Authorized to Offer Degree:

Electrical and Computer Engineering

University of Washington

Abstract

Design and Characterization of Optical Metasurface Systems

Elyas Bayati

Chair of the Supervisory Committee:
Professor Arka Majumdar
Electrical and Computer Engineering

The importance of optics is increasing in our daily lives, from medical devices to the cameras that facilitate global communications. Because of their universal use, the size, scale and quality of optical elements grow in importance for technological innovations. Over the last few decades, the downscaling of complementary metal–oxide–semiconductor (CMOS) sensors thanks to Moore's law have resulted in a dramatic reduction in the size of optical systems, including imaging and non-imaging systems. However, most optical systems are now limited in size by the optical element itself, not the sensor. One promising candidate for enabling further miniaturization is metasurfaces, which are ultrathin elements comprising arrays of subwavelength-spaced scattering elements. These metasurface elements can achieve a broad class of functionalities in a flat form factor, transforming the phase, amplitude, and polarization of incident electromagnetic radiation. While metasurfaces provide a large number of degrees of freedom to design complex optical

functions, their full potential and applicability have yet to be discovered. This dissertation will investigate a variety of different metasurface designs and expand on the functionality of these optical elements as solutions for imaging and non-imaging systems.

In the body of this dissertation, we investigated how to design dielectric metasurface subwavelength scattering elements to optimize them for a variety of functions. The designs discussed represent the research progress made towards developing optical sensors for imaging and non-imaging systems that are more compact. In particular, this Thesis highlights designs for silicon nitride based scattering elements for 1D and 2D EDOF metasurfaces in the visible regime for full color imaging. This is followed by a more general methodology that uses EDOF lenses in conjunction with computational imaging to eliminate broadband chromatic aberrations. Lastly, there are proposed designs for composite metasurface visors that can overcome several challenges of near eye augmented reality visors, including reducing bulkiness, addressing FOV limitations, minimizing chromatic aberrations and improving the see-through quality. The demonstrated approach may find applications in microscopy, planar cameras, medical imaging, and augmented reality.

TABLE OF CONTENTS

ACKNOWLEDGEMENTS

I would like to express my gratitude to my advisor Prof. Arka Majumdar, who is an inspiring mentor and passionate scientist. I am so grateful for his guidance and support over the past five years. He was supportive in all aspects, including with my immigration visa challenges, with connections to the industry, and also finding a new path for my research. Especially, in my first couple years, he knew about every detail of my projects and always offered guidance whenever I was stuck. Arka also encouraged me to present at conferences and take three internship opportunities that significantly furthered my career. More importantly, besides the scientific ideas that I learned from him, I am deeply inspired by his confident and optimistic attitude towards research and everyday life, which I believe will continue to influence me even after graduate school.

During my PhD, Shane Colburn always supported me and also discussed new ideas with me. He was very helpful in teaching me new optics concepts and also a good role model to follow as a senior student in our lab. In addition to that, he was a great friend to talk with about anything in life. I am grateful that he was part of this journey with me. I also would like to thank Alan Zhan. When I joined the group, he was the most senior student of the lab, and he conveyed his experience to me and also motivation to pursue my research.

During my PhD, I also had a lot of great colleagues, and lab mates to work with and learn from including, Albert Ryou, James whitehead, Yueyang Chen, Abhi Saxena, Roger Fang, Jiajiu Zheng, Shreyas Shah. I would also like to thank James whitehead, Quentin Tanguy who helped me a lot with fabrication and new ideas in the nano fabrication facilities. I have a lot of appreciation for the help that I got from Maksym (Max) Zhelyeznyakov, Loucheng Huang and Andrew wolfram with a lot of theoretical problems. They are sharp and great scientist to discuss computational problems with.

I am so grateful with the staff at the Washington Nano Fabrication facility at UW. They helped me a lot to facilitate my research in terms of fabrication. I am also thankful to John Martin who helped me with funding for one of my projects during my PhD. His generosity made that project possible.
I also want to thank Prof. Hassan Arbab. I started my grad school in Electrical Engineering department at University of Washington in fall 2015 with him and I spent first year of my master program with him.
I especially want to thank my family for their unconditional support and encouragement throughout my education. My mom has always been supportive of no matter what path I have taken. My grandparents and siblings have always encouraged and inspired me to do more. I want to give an enormous thanks to my friends and my girlfriend for their love and support throughout the past few years. Whenever I was vexed by something, stressed, or perplexed by difficult decisions, they were a great listener and always gave good advice.

Chapter 1. INTRODUCTION

1.1 MOTIVATION

The importance of optics is increasing in our daily lives, from medical devices to the cameras that facilitate global communications. Because of their universal use, the size, scale and quality of optical elements grows in importance for technological innovations. Over the last few decades, the downscaling of complementary metal–oxide–semiconductor (CMOS) sensors via Moore's law have resulted in a dramatic reduction in the size of optical systems, including imaging and non-imaging systems. However, most optical systems are currently limited in size by the optical element itself, not the sensor.

The large size and bulkiness of conventional optical elements present many challenges for technological innovations, and these challenges are magnified by the growing complexity of optical systems. Today, technological solutions often require a higher level of functionality and efficiency in all aspects of their design. For many fields, the existing cumbersome optics present significant barriers to progress. Indeed, there are a multitude of applications for miniaturized and multi-functional optical systems. Aside from other components, simply reducing the size of cameras can have many useful imaging applications, especially in the field of medical and brain imaging which could improve health outcomes with the development of implantable microscopes, endoscopes and angioscopes. There are also many applications in the realm of augmented or virtual reality, which struggle with the heaviness and size of depth cameras. With advances in camera miniaturization, augmented reality could be made much more practical for use in education and entertainment.

A vital first step towards miniaturization in optics was the development of the composite compact lens for lighthouses by Augustin-Jean Fresnel. Building on Fresnel's observations that the function of the lens is determined by the curvature, we are able to eliminate a significant portion of the bulk. By reshaping the surface and removing much of the curved portion of the lens, we are left with just the amount of glass necessary to focus the image. However, while this approach reduces the weight and amount of material required for a lens, using this older method to remove excess material ultimately comes at the expense of the lens's imaging performance.

In the evolution of optics technology, the development of Fresnel lenses was followed by the design of diffractive optics, which alter lenses to interact directly with the wave character of light. Diffractive optics are characterized by the way they act on the amplitude, or phase of an incident beam of light, interrupting its curve at designated points. Within the family of diffractive optics there are metasurfaces. These are a special case of phase controlling diffractive optics, with two defining qualities: they have subwavelength periodicity, and they are compatible with binary lithography. Because they facilitate the function of lenses by altering the texture of the surface at a nanophotonics scale, metasurfaces are uniquely positioned to aid in the miniaturization of optics, removing a significant barrier for innovations in the fields previously mentioned, and many more. In the next chapter, I will expand on the qualities of metasurfaces.

1.2 METASURFACES

Dielectric metasurfaces, two-dimensional quasi-periodic arrays of subwavelength scatterers have recently emerged as a promising technology to create ultra-thin, flat and miniature optical elements [1]. With these sub-wavelength scatterers, metasurfaces shape optical wavefronts, modifying the phase, amplitude, and/or polarization of incident light in transmission or reflection. Many different optical components such as lenses [2, 3], focusing mirrors [4], vortex beam

generators [5, 6], holographic masks [7, 8], polarization optics [9, 10] and freeform surfaces [11] have been demonstrated using metasurfaces. While metasurfaces provide an extremely large number of degrees of freedom to design complex optical functions, our intuition often fails to harness all these degrees of freedom. In this dissertation, I will investigate a variety of different metasurface designs, and expand on the functionality of these optical elements as solutions for imaging and non-imaging systems.

1.3 THESIS OUTLINE

The research goal of my graduate work centered on the development of improved optical metasurface systems. These advanced metasurface systems have both imaging and non-imaging applications and outperform previous metasurface designs. In this dissertation, I am going to talk about my development progress in three chapters. Following this introduction, chapter two starts by exploring the limitations of these systems in terms of material of choices available, and their varied utility. Although metasurfaces can be applied to a variety of optical elements, my research focused on metasurfaces for lenses (metalenses). Metalenses are the optimal element for my research because their performance can most easily be compared to other existing metasurface designs. Chapters three and four, discuss the imaging and non-imaging applications of two optical metasurface systems. Starting in chapter three, I detail efforts to build an extended depth of focus (EDOF) metasurface lens in both a one- and two-dimensional (1D and 2D) domain, illustrating design advances that improve full color imaging systems. Chapter four follows with my discussion of metasurface design for a more complex non-imaging system such as augmented reality and virtual reality glasses. Such applications gain clear benefits from miniaturization using

metasurfaces. Lastly, chapter five contains my concluding remarks on all the topics discussed in the preceding chapters.

Chapter 2. CHOICE OF MATERIAL

This section is adapted with permission from [123], *Bayati, E., Zhan, A., Colburn, S., Zhelyeznyakov, M. V., & Majumdar, A. (2019). Role of refractive index in metalens performance. Applied Optics, 58(6), 1460-1466.* © The Optical Society.

2.1 INTRODUCTION

Metasurfaces initially relied on deep-subwavelength metallic structures and operated at mid-infrared frequencies [1]. The large absorption loss in metals made it difficult to create high-efficiency metasurface devices in the visible and near-infrared (NIR) wavelengths. This motivated the fabrication of metasurfaces using dielectric materials because of the low optical loss of dielectrics at visible and NIR wavelengths. While initial research focused on higher-index amorphous silicon (Si) [3, 12] at NIR wavelengths, recently materials with lower refractive index, such as titanium oxide (TiO_2) [13], gallium nitride (GaN) [14], and silicon nitride (SiN) [15, 16] have been used to create metasurfaces operating at visible wavelengths. Based on the empirical Moss relation $n^4 \sim 1/E_g$ [17] with refractive index n and the electronic bandgap E_g, we expect that a large optical transparency window necessitates the material refractive index to be lower. Hence, to create metasurfaces at shorter wavelengths, we have to rely on materials with lower refractive index. In decreasing the refractive index, however, it is unclear what effect there will be on the device performance. Recently, the efficiency of a periodic meta-grating was analyzed at optical frequency as a function of the material refractive index [18]. They reported that for large deflection

angles the efficiency decreases with lower refractive index, but for low deflection angles there is no significant difference in efficiency of transmissive thick meta-gratings made of different materials. While this analysis with periodic structures can help qualitatively understand the performance of a metasurface lens (metalens) with quasi-periodic arrangements of scatterers [19-21], a systematic and quantitative evaluation of material selection for metalenses is currently lacking. It is unclear what the minimum required dielectric contrast is to achieve high-efficiency and high numerical aperture metalenses. Answering this is vital for understanding the capabilities, limitations, efficiency, and manufacturability of metalenses over a specific wavelength range. We note that, the effect of refractive index is explicit in the lens maker's formula [22] for a refractive lens:

$$\frac{1}{f} = (n-1)\left(\frac{1}{R} - \frac{1}{R'}\right)$$

where f is the focal length, n is the refractive index of the lens, and R and R' are the radii of curvature of the two spherical surfaces of the lens. The angle of refraction, and therefore the focal length depends on the curvature of the lens surface and the material used to construct the lens. However, for metalenses, there is no study or theoretical formula relating the refractive index to the focal length or numerical aperture and the efficiency. In this chapter, we design and analyze metalenses made of materials with wide range of refractive indices to estimate the relationship between refractive index and performance of metalenses. We analyze metalenses operating in the near infrared spectral regime (λ = 1550nm) in terms of efficiency and full width at half maximum (FWHM). We consider six different dielectric materials: Si (n = 3.43) [3], TiO_2 (n = 2.4) [13], GaN (n = 2.3) [14], SiN (n = 2.0) [15, 16], SiO_2 (n=1.5) [23] and an artificial material with a refractive index of 1.2. The index range under n=2 is of particular importance as large-scale printable photonics technology, which is promising for low-cost manufacturing of metasurfaces,

requires the refractive index to be near 1.5 [24]. First, we used a forward design technique based on rigorous coupled-wave analysis (RCWA) [25, 26] followed by finite-difference time-domain (FDTD) simulations [3, 15]. We compare the focusing efficiency and FWHM at the focal-plane as a function of the numerical aperture for different materials. We then employed inverse electromagnetic design based on generalized Mie scattering theory and adjoint optimization [27] to calculate the dependence of metalens performance and FWHM at the focal plane on refractive indices between 1.25 and 3.5.

2.2 Forward Design Method

The main building block of a metalens is a scatterer arranged in a subwavelength periodic lattice (with a period p). Here, we assume the scatterers to be cylindrical pillars, arranged in a square lattice, as shown in Figure 1. Since we have sub-wavelength periodicity in a metalens, only the zeroth-order plane wave propagates a significant distance from the metasurface, and other higher order diffracted plane waves are evanescent [28]. This makes metalenses more efficient compared to other diffractive optics.

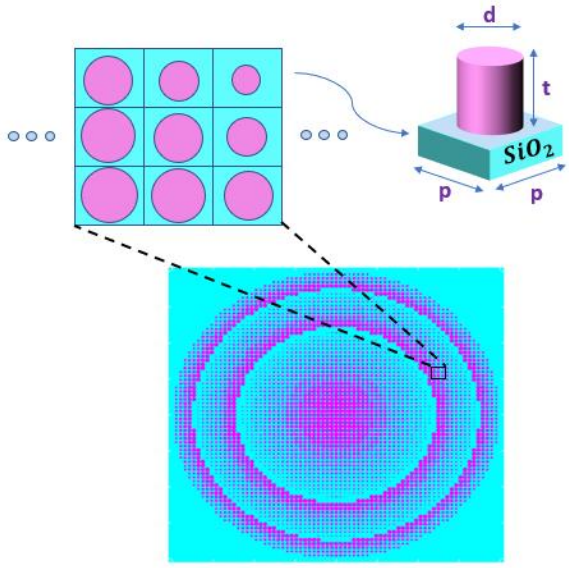

Figure 1. Schematic of a metalens and its lattice structures: a lattice with periodicity p can be formed by using cylindrical pillars (with diameter d and thickness t) on top of a silicon dioxide substrate, arranged in a square lattice. By varying the radius of the cylindrical pillars, we can impart different phase-shifts.

Forward design of a metalens involves selecting the appropriate spatial phase profile for the specific optical component, arranging the scatterers on a subwavelength lattice, and spatially varying their dimensions. To have an arbitrary transmission phase profile, phase shifts of scatterer should span the 0 to 2π range while maintaining large transmission amplitudes. In our simulation, we used the phase-profile of metalens as:

$$\phi(x,y) = \frac{2\pi}{\lambda}\left(\sqrt{x^2+y^2+f^2} - f\right)$$

We discretize this continuous spatial phase profile onto a square lattice with periodicity p , giving us a discrete spatial phase map with different phase values. We then quantize the phase profile with ten linear steps between 0 and 2π, corresponding to ten different pillar radii. For each value of this new discrete spatial phase profile, we find the radius of the pillar that most closely reproduces that phase and place it on the lattice.

The complex transmission coefficient of a zeroth-order plane wave depends upon the lattice periodicity p, scatterer dimensions (both the diameter d and thickness t), and refractive index n. Using RCWA, we calculate the transmission phase and amplitude of the scatterers as a function of duty cycle (d/p) for different materials assuming a periodic boundary condition (Figure 2). For different refractive indices, we can find several sets of thickness t and lattice periodicities p that provide a full 0 to 2π phase shift range under varying diameters while maintaining high transmission amplitude (transmissivity ~1). Some resonant dips in transmission are observed, which can be attributed to guided mode resonances [29]. Metasurface parameters, including lattice periodicity p and thickness t, for each material are shown in Table 1. As we are comparing different materials, we chose these parameters to maintain the same thickness to period ratio across simulations, in this case selecting $t/p \sim 1.6$. For our artificial material with refractive index of 1.2, however, in order to cover the whole 0 to 2π phase shift range, we need to increase the thickness. To keep the same thickness to period ratio, we cannot maintain sub-wavelength periodicity. Hence, for n=1.2, we assume a thickness to period ratio of 3.6 to get the maximum possible phase shift. We assume the substrates for all materials to be SiO_2 with a thickness $t_{sub} = \lambda$. We also note that, some of the parameters reported in this paper, will be difficult to fabricate. However, in this paper, we primarily want to understand the dependence of the metalens performance on the refractive index, and experimental feasibility is not considered.

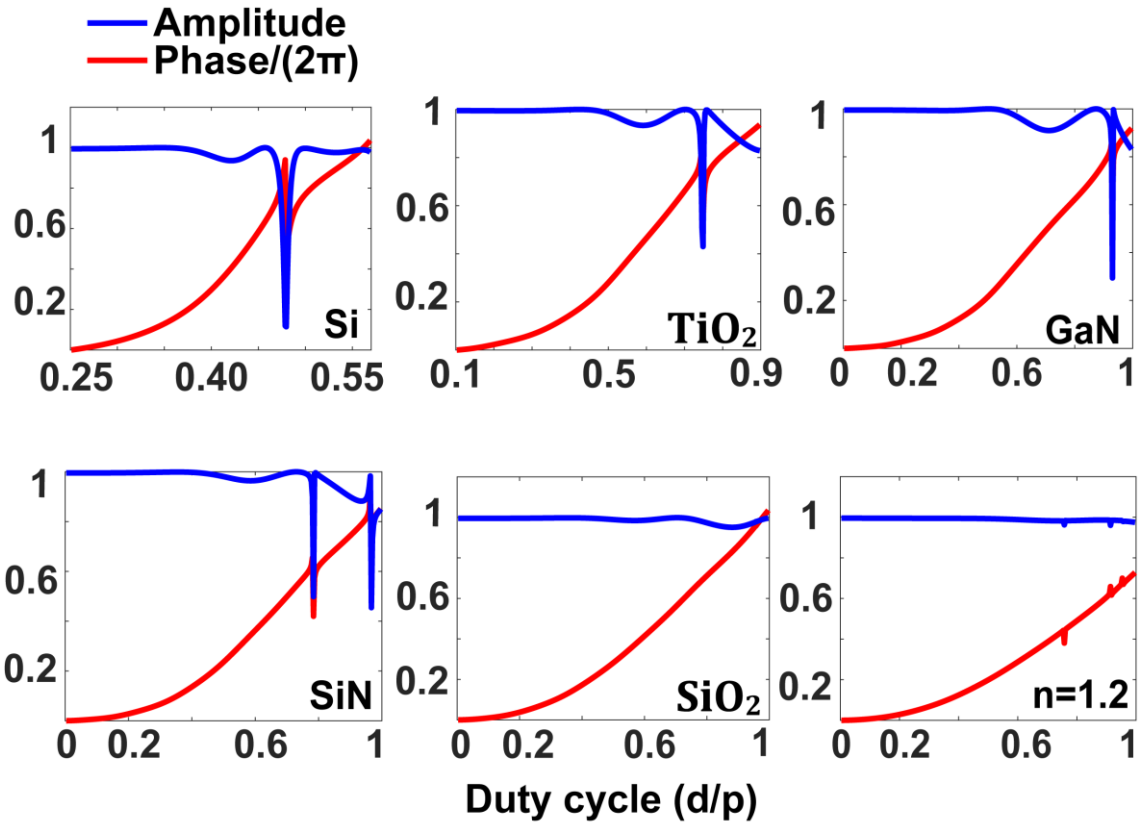

Figure 2. Amplitude and phase of the transmitted light through a scatterer: using RCWA, we calculate the transmission properties (red: phase delay; blue: transmission amplitude) as a function of the ratio of the pillar diameter and periodicity. We kept the thickness to period ratio, i.e., the ratio between the thickness and the periodicity same for all materials except for n=1.2 to compare their efficiency.

Using the parameters obtained from RCWA, we designed arrays of nanopillars and simulated the metalenses using Lumerical FDTD solutions. The pillar diameters corresponding to resonances in Figure 2 are excluded when designing the metasurfaces to get higher efficiency. We analyzed the performance of the metalenses in terms of FWHM and focusing efficiency for different focal lengths ($5 - 200\mu m$). The diameter of the metalenses is kept constant at 80 μm.

Table 1. Metasurface parameters including lattice periodicity p and thickness t for each refractive index, which are used in forward design method (optical wavelength $\lambda = 1550nm$.)

Refractive index (n)	Si ($n = 3.43$)	TiO_2 ($n = 2.4$)	GaN ($n = 2.3$)	SiN ($n = 2$)	SiO_2 ($n = 1.5$)	($n = 1.2$)
Periodicity (p)(nm)	775	790.5	759.5	930	1372	1395
Thickness (t)(nm)	1240	1317	1240	1550	2290	5022

The FWHM of the focal spot is shown in Figure 3a as a function of numerical aperture, where the solid black curve is the FWHM of a diffraction-limited spot of a lens with the same geometric parameters. There is no appreciable difference in the FWHM across the range of simulated indices, except for n=1.2, where the FWHM does not decrease at very high numerical apertures. We define the focusing efficiency as the power within a radius of three times the FWHM at the focal plane to the total power incident upon the lens [3, 15]. Figure 3b shows the focusing efficiency as a function of refractive index of all materials for different numerical apertures. We find that the focusing efficiency decreases with higher numerical apertures, as observed before [3, 15]. At low numerical apertures ($NA < 0.6$), the efficiency of the metalenses is almost independent of the material refractive index. The decrease in the efficiency with increasing numerical aperture, however, is more drastic with lower refractive index, and the efficiency drops more quickly in materials with refractive indices below 1.5.

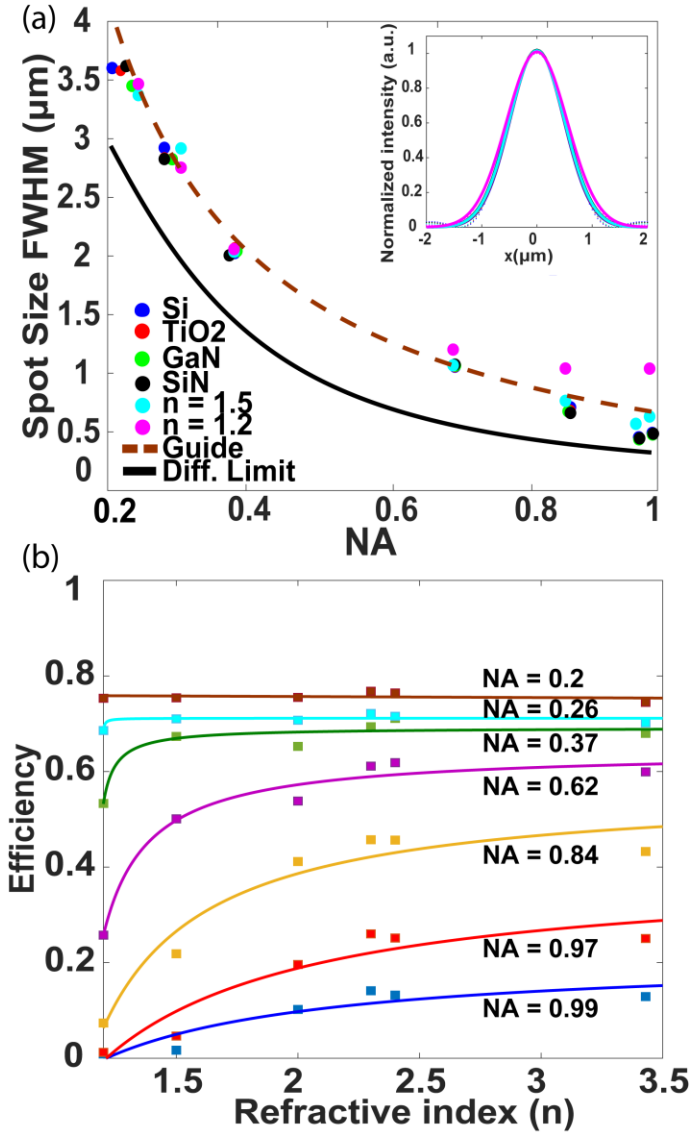

Figure 3. Performance of the metalens designed using forward design methodology: (a) The FWHM of the focal spot is plotted as a function of numerical aperture of the lens. Inset plot of (a) shows cross-section of the beam size for focal length of 50 μm with their Gaussian fit functions. The solid and dashed curves are the diffraction-limited FWHM, and guide to the eye, respectively. (b) The efficiency of metalenses for all materials as a function of refractive index for each numerical aperture using forward design method.

2.3 INVERSE DESIGN METHOD

In the forward design method, we kept the thickness to period ratio (t/p) of the scatterers fixed for different materials. This constraint restricts the design space and makes it difficult to objectively compare metalenses made of different materials. Furthermore, the local phase approximation that we make in going from RCWA to FDTD neglects the coupling between the scatterers. Such coupling is not negligible when the material refractive index is small. We also had to manually inspect the data from RCWA to determine the quality of the parameters and avoid resonant dips before constructing the FDTD simulation. We can circumvent these problems by employing an inverse electromagnetic design methodology developed by our group [27].

Recently, inverse electromagnetic design has been applied to phase profile design [7], single scatterer design [30], beam steering [31], and achromatic metasurface optics [32, 33]. We utilize an inverse design method utilizing adjoint optimization-based gradient descent and multi-sphere Mie theory which describes the scattering properties of a cluster of interacting spheres. We determine the interactive scattering coefficients for each sphere individually, similar to what Mie theory does for a single sphere [34, 35]. In our inverse design, we do not make any assumption about the size of our scatterers, but we fix their periodicity. Consequently, we expect to explore a larger design-space to find well-suited parameters for our metalens. Our simulation tool also aims to design the whole metasurface and not just the unit cell, and thus the coupling between scatterers is already included in the design process.

Our inverse design method based on Mie scattering, however, currently only works for spherical scatterers. Hence, in our design, we optimize the radii of different spheres. The radii and periodicity of the metalenses are chosen to avoid any physical overlap or contact between adjacent spheres. We run the optimization routine up to a fixed number of iterations (in this case 100) to

obtain the final metalens. The iteration time of the inverse design method depends on both the particle number and the expansion order of the orbital index l. The expansion order here provides the number of spherical basis functions for each particle to include in our simulation [27]. Larger numbers of particles and expansion orders increase the iteration time. As we are interested in sub-wavelength structures to design metalenses, it is important to find a reasonable cut-off for the expansion order to balance the speed of the iteration, and the accuracy of the result. The valid cutoff expansion order (l_{max}), which is ultimately determined by the physical size and refractive index of the individual spheres relative to the incident wavelength, is chosen to be 3 in our simulations. Since these scattering properties are determined by the geometric and material properties of the sphere in addition to the wavelength of the incident light, there is a relation between cutoff expansion order and possible periodicity range of the scatterers. Here, the periodicities of the metalenses are chosen in a way such that the contribution from expansion orders greater than 3 are negligible.

Table 2. The periodicity values for ten different refractive indices, which are used in inverse design method

Refractive index (n)	**Periodicity** $(p)(nm)$	**Refractive index** (n)	**Periodicity** $(p)(nm)$
1.25	1360	**2.5**	1020
1.5	1330	**2.75**	976
1.75	1222	**3**	912
2	1140	**3.25**	838
2.25	1122	**3.5**	800

We chose ten equally spaced refractive indices between n= 1.25 to n=3.5 for the inverse design. We assume a square periodic lattice, where the spheres with different radii are placed. For all simulations, we assume the spheres are suspended in vacuum, and do not include a substrate. Initially, all the spheres have identical radii. We then allow the sphere radii to vary continuously between 150 nm and half of the periodicity to optimize the figure of merit, which is the intensity at the designed focal point. The periodicities for all refractive indices for the inverse design method are shown in Table 2. The final radii distribution of the optimization process for one metalens using inverse design method is shown in Figure 4. We find that the result is mostly rotationally symmetric as expected for a lens. We attribute the slight asymmetry near the origin to our optimization running for a fixed number of iterations and converging at a local minimum. The radius of the designed metalenses is 20 μm, and five focal lengths between 15 μm and 100 μm are tested to provide us the same number of numerical apertures for better comparison with the forward design.

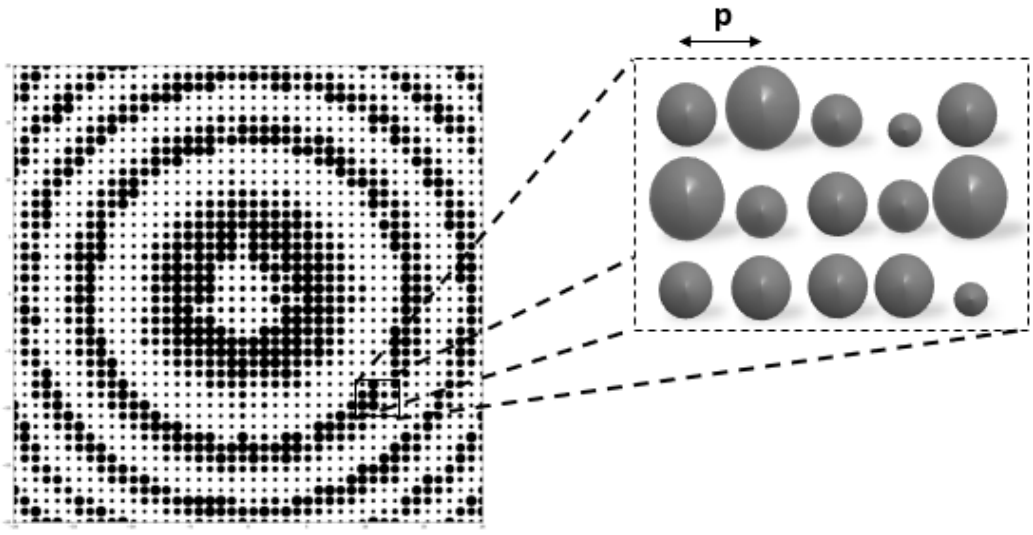

Figure 4. Final radii distribution of a metalens using inverse design method. Spheres are arranged in a square lattice with periodicity p. Radii of spheres are allowed to range from 150 nm to the half of the periodicity.

The FWHM of the focal spots of the metalenses are shown in Figure 5a as a function of the numerical aperture, where the solid black curve is the FWHM of a diffraction-limited spot of a lens with the given geometric parameters. Like the forward design method, there is no appreciable difference in the FWHM across the range of simulated indices, except at n=1.25, where the FWHM does not decrease at very high numerical apertures. At lower numerical apertures, however, we observe FWHM's smaller than those a diffracted-limited spot. We emphasize that this is not truly breaking the diffraction limit, but rather we attribute this to a larger proportion of the light intensity being located within side lobes as opposed to within the central peak. By shifting power from the central peak to the side lobes, beam spot sizes that are less than the diffraction-limited spot size are possible [36]. This shifting of light to the side lobes may have arisen from the defined figure of merit, in which we did not enforce a condition on the beam spot size and side lobe intensity ratio. The efficiencies of these metalenses are plotted as a function of their refractive indices in Figure 5b, where the different numerical apertures are specified with different colors. We find that the focusing efficiency decreases with increasing numerical aperture. According to Figure 5b, there is no significant difference in the focusing efficiency of high and low refractive index materials for low numerical apertures in the range of $NA = 0.2 - 0.37$ (50 – 100 μm focal length). For longer numerical apertures, however, such as 0.62 and 0.8, larger refractive index materials provide higher focusing efficiency.

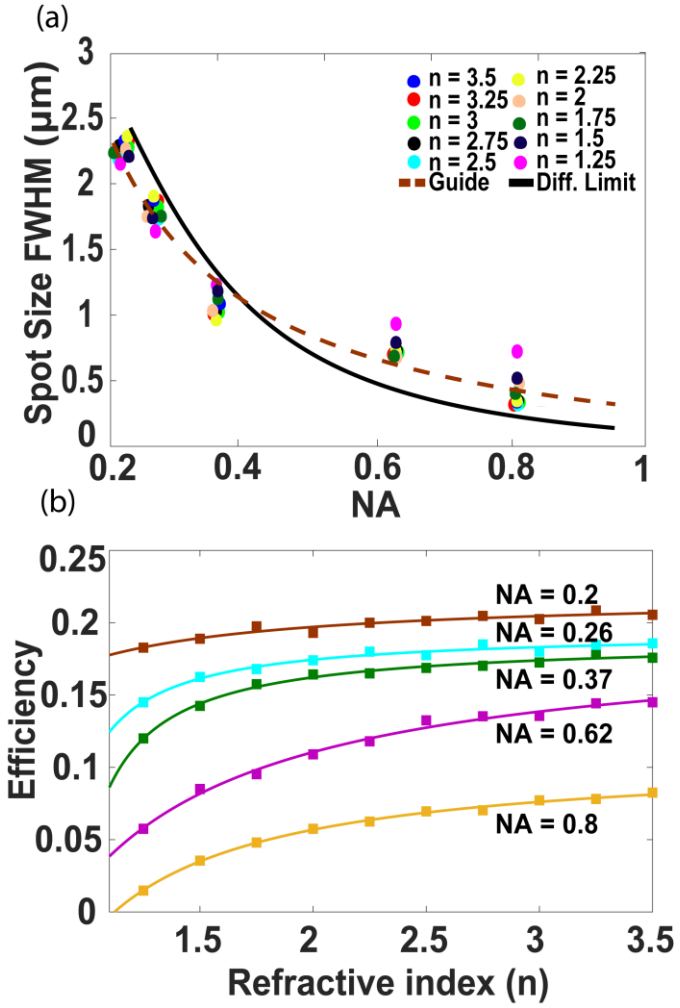

Figure 5. Performance of the metalens using the inverse design method: (a) The FWHM of the focal spot as a function of numerical aperture of the lens. The solid and dashed curves are the diffraction-limited FWHM, and guide to the eye, respectively. (b) shows the focusing efficiencies of metalenses with different numerical apertures against material refractive indices in the 1.25 to 3.5 range using the inverse design method. Different numerical apertures are specified with different colors and plotted curves are guides to the eye.

2.4 DISCUSSION

A consistent behavior is observed between forward design (Figure 3) and inverse design (Figure 5) regarding the relation between the focusing efficiency of metalenses and their refractive index. For lower numerical apertures, there is no significant difference in focusing efficiency of metalenses with refractive indices in range of 1.25 to 3.5. However, for higher numerical apertures, achieving higher focusing efficiency metalenses is feasible by increasing their refractive index.

On the other hand, focusing efficiencies for metalenses with different numerical apertures using the inverse design method are much smaller than the ones in forward design method. To understand why we have such a reduction in focusing efficiency, we calculated the transmission phase and amplitude of the spherical scatterers as a function of duty cycle (d/p) for SiN as a sample material, assuming a periodic boundary condition (Figure 6) and found that they cannot provide a full 0 to 2π phase shift range under varying diameters of sphere while maintaining high transmission amplitude. As these spheres are the main building block of metalenses in inverse design method, we cannot achieve high focusing efficiency for metalenses based on spherical scatterers. However, these results show that, the same trend between forward design (Figure 3) and inverse design (Figure 5) regarding the relation between the focusing efficiency of the metalenses with the refractive index is not due to the actual phase or scatterer geometry, but inherently dependent on the refractive index. Also, the FWHM of the focal spots from the inverse design method are smaller than those in the forward design method. We attribute this to our choice of figure of merit, for which we did not enforce a condition on the beam spot size.

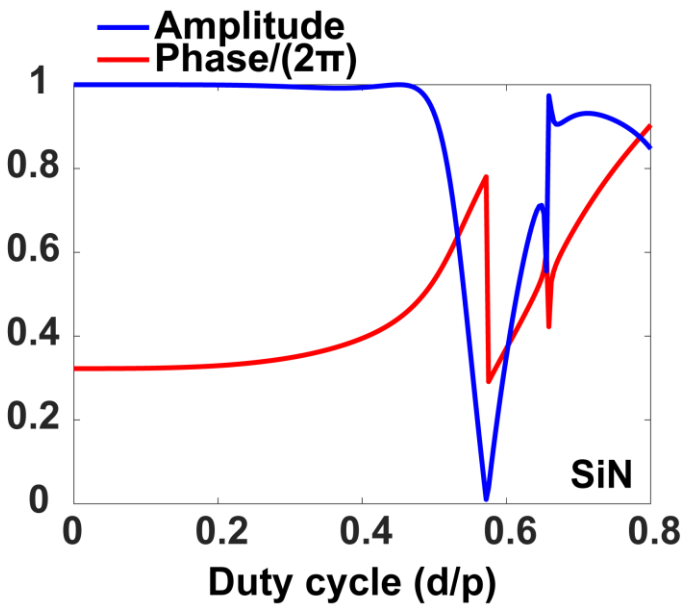

Figure 6. Amplitude and phase of the transmitted light through a spherical scatterer: using RCWA, we calculate the transmission properties (red: phase delay; blue: transmission amplitude) as a function of the ratio of the sphere diameter and periodicity.

The performance of a metalens is related to that of a metasurface beam deflector, whose performance as a function of material refractive index was recently analyzed at optical frequencies [18]. It was shown that while over 80% efficiency can be obtained using high contrast materials such as Si and Ge, for large-angle ($> 60^o$) beam deflection, the efficiency drops quickly for low index materials, such as SiN. However, no significant difference in efficiency for modest deflection angles ($< 40^o$) was observed for different materials. Such behavior is justified by coupled Bloch-mode analysis [18, 37]. This finding is consistent with our result that for high numerical aperture metalenses, higher refractive index materials provide higher efficiency but at low numerical apertures there is no significant difference in performance.

We have evaluated low-loss dielectric materials with a wide range of refractive indices for designing metalenses using both forward and inverse design methodologies. We found reasonable agreement between both methods in terms of the focusing efficiency and the FWHM of the focal

spots on the material refractive indices. We found that for low numerical apertures ($NA < 0.6$), the efficiency of the metalenses is almost independent of the refractive index. For higher numerical apertures, however, high-index materials provide higher efficiency. The relationship between refractive index and metalens performance is significant in choosing appropriate material, based on considerations like ease and scalability of manufacturing, or better tunability. In addition, we show that, even with very low refractive index ($n < 2$), we can achieve reasonable efficiency in a metalens, which will be significant for enabling fabrication with printable photonics technologies.

Chapter 3. EDOF METASURFACE SYSTEMS

The material in this chapter was in part presented in [124-125],

[124] Bayati, E., Pestourie, R., Colburn, S., Lin, Z., Johnson, S. G., & Majumdar, A. (2020). Inverse designed metalenses with extended depth of focus. ACS photonics, 7(4), 873-878. Copyright 2020. American Chemical Society.

[125] Bayati, E., Pestourie, R., Colburn, S., Lin, Z., Johnson, S. G., & Majumdar, A. (2021). Inverse designed extended depth of focus meta-optics for broadband imaging in the visible. Nanophotonics.

3.1 1D EDOF METALENSES

Metasurfaces provide an extremely large number of degrees of freedom to design complex optical functions, however, our intuition often fails to harness all these degrees of freedom. One promising solution is to employ computational techniques to design metasurfaces, where the design process starts from the desired functionality, and the scatterers are designed based on a specified figure of merit. Such design methodologies, often referred to as inverse design, have been employed to design high efficiency periodic gratings [38, 39], monochromatic lenses [40, 41], PSF-engineered optics [42] and achromatic lenses [43-45]. The inverse design is important because it could outperform the conventional approach for the design of metasurfaces, specifically, when desired function is not possible to design with conventional method. Till date, however, there are limited experimental demonstrations of inverse-designed aperiodic metasurfaces exhibiting superior performance to optics designed by traditional methods. For example, recently demonstrated inverse-designed cylindrical lenses exhibit high efficiency [46], though the efficiency is not higher than that of a traditional refractive lens.

Extended depth of focus (EDOF) lenses represent an important class of optical elements, with significant utility in microscopy [47] and computational imaging [48]. This class of lenses differs from an ordinary lens, as the point spread function (PSF) of the lens remains the same over an extended distance along the optical axis. EDOF lenses not only enable novel functionalities, such as bringing objects at different distances away from the lens into focus but also alleviate the stringent requirements on aligning lenses on top of a sensor. While for an ordinary lens the gap between the lens and the sensor plane needs to be very close to the focal length, with EDOF lenses, the gap can vary to a degree without sacrificing the performance of the imaging system. In recent years, metasurfaces have been employed to implement two-dimensional EDOF lenses [49, 50]. Existing EDOF lenses, however, have several problems. One of the most prevalent classes of EDOF lenses is created via a cubic phase mask positioned at the exit pupil [47]. Such an approach generates an Airy beam, which propagates through free space without significant distortion. The resulting PSF, however, does not resemble a point, and images captured with this element are therefore blurry. Computational reconstruction is required to undo the distortion. Another option could be to use a log-asphere lens or other variants [51]. For these lenses, however, different parts of the lens focus at different depths, significantly limiting the focusing efficiency. In one dimension, several works theoretically explored cylindrical EDOF lenses [52-55], although to the best of our knowledge no experimental demonstration has previously been reported.

In this section, we design and fabricate an EDOF cylindrical metasurface lens (metalens) using an inverse electromagnetic design methodology. Unlike existing implementations of diffractive or refractive EDOF lenses, the reported metalens creates a lens-like PSF, without introducing significant blur like many other EDOF lenses. We designed the EDOF lens to have three times the depth of focus of an ordinary metalens. The design is experimentally validated by

fabrication and optical characterization. We found reasonable agreement between the simulated and experimental results in terms of the focusing efficiency and the FWHM of the focal spots. The depth of focus of the inverse designed metalens is extended by a factor of ~1.5-2 over that of the traditional metalens. We also did not observe any degradation of the efficiency in the designed EDOF lenses.

3.1.1 *Inverse Design and Validation*

The depth of focus Δf of an ordinary lens with diameter D and focal length f, for optical wavelength λ is given by

$$\Delta f = 4\lambda \frac{f^2}{D^2}$$

We aim to demonstrate an EDOF metalens with a depth of focus of three times this value. We specify our figure of merit (FOM) as the intensity at eight linearly spaced points along the optical axis which cover an interval of length $3 \times \Delta f$ and that are centered around the focal length. We use max-min multi-objective optimization [56] to maximize the intensity uniformly on the segment. We optimize the EDOF lens FOM by adjusting the widths of 150 nano-stripes positioned at the center of each lattice cell. The material of the metasurface is assumed to be silicon nitride (n~2). The lattice periodicity and thickness of the metasurface are kept constant at 443 nm and 600 nm, respectively. The choice of these parameters is dictated by the ease of fabrication, such as the total area of fabrication and reproducibility of the feature sizes. To ensure the fabricability of the designed metasurface, we constrain the minimum width of the stripes to 100nm. Lenses with three different focal lengths (66.66 μm, 100 μm, 133.33 μm) are designed. To channel most of the light into the main lobe, i.e., to reduce the sidebands in the focal length we ran the inverse design with different initial conditions, which resulted in several different geometries. We then chose the

design with the least power in the sidebands. In contrast to a traditional lens, the inverse problem of designing an EDOF lens has multiple solutions to Maxwell's equations that could be good candidates for the EDOF design. Our inverse design framework enables us to set the problem without constraining ourselves to just one of these solutions. Note that if our design method was based on optimizing a phase mask instead of solving for the geometry of our scatterers directly, we would be limited to a single solution, which would be suboptimal in the sense that it limits the degrees of freedom. We note that, however, an inverse design method, where the refractive index of each voxel in the structure are used as degrees of freedom can potentially provide a better solution, albeit with significantly increased computational time. As such, the inverse design method employed here provides a good trade-off between an improved design and computational complexity.

3.1.2 *Experimental Demonstration*

To validate our metasurface design, we fabricated the cylindrical metalenses in silicon nitride. A 600-nm-thick layer of silicon nitride was first deposited on a 500-um-thick fused-silica substrate using plasma-enhanced chemical vapor deposition (PECVD). The sample was then spin-coated with electron-beam resist (ZEP-520A) and then the metalens' patterns were exposed via electron-beam lithography. 8-nm of Au/Pd as a charge dissipation layer was sputtered on the resist prior to exposure to prevent pattern distortion due to electrostatic charging. After the lithography step, the charge dissipating layer was removed by type TFA gold etchant and the resist was developed in amyl acetate. A 50 nm layer of aluminum was then evaporated onto the sample. After performing lift-off, the sample was etched using an inductively coupled plasma etcher with a mixture of CHF_3 and O_2 gases, and the remaining aluminum was removed in AD-10 photoresist developer. To demonstrate the extension of the depth of focus, we fabricated two sets of lenses:

one set of ordinary metalenses designed via the forward design method and another set of EDOF metalenses developed using our inverse design method. The forward design method of a metalens involves selecting the appropriate spatial phase profile for the specific optical component, arranging the scatterers on a subwavelength lattice, and spatially varying their dimensions. Whereas, in the inverse design, no a priori knowledge of the phase distribution is assumed, and the metalens is designed via optimizing the FOM. Figs. 7A, B show the scanning electron micrograph (SEM) of the fabricated EDOF metalens (using inverse design method) and traditional metalens (using forward design method), respectively. Figs. 7C, D show a zoomed-in SEM of the inverse-designed EDOF metalens, which shows silicon nitride nano-stripes forming the cylindrical EDOF metalens. We fabricated three metalenses corresponding to three different focal lengths, in each set. The fabricated lenses were measured using a confocal microscopy setup under illumination by a 625 nm light-emitting diode (part number Thorlabs-M625F2), see Fig. 7E.

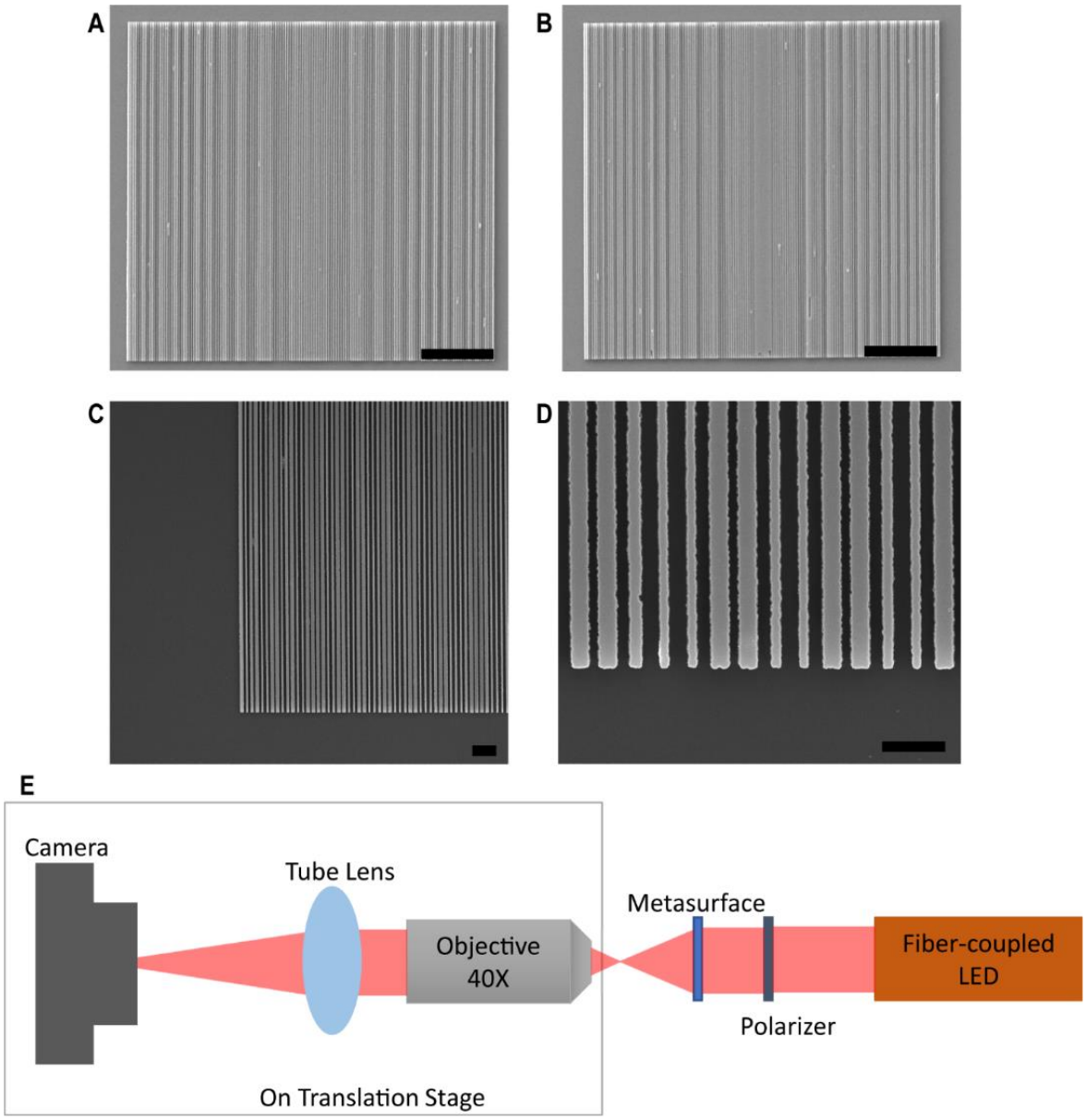

Figure 7. Scanning electron micrograph (SEM) of (A) inverse-designed EDOF metalens, (B) traditional metalens; (C) and (D) Zoom-in SEM on inverse-designed EDOF metalens which shows silicon nitride stripes forming the cylindrical EDOF metalens; The scale bars correspond to 10 μm (A-B) and 1 μm (C-D), (E) Confocal microscopy setup used to measure the metalenses.

Figs. 8A-F show the simulated and experimentally measured field profiles for the three inverse-designed EDOF metalenses. The field profiles are simulated using 2D finite-difference time-domain (FDTD) simulation with an axial sampling resolution of 50 nm. The intensity profiles along the optical axis are captured using a camera and translating the microscope along the optical axis using an automated translation stage with an axial resolution of 2 μm. We find that the simulated field profiles from the designed structures match quite well with the experimentally measured focusing behavior. A clear elongation of the focal spot along the optical axis is observed. We also characterized the performance of inverse-designed EDOF metalens under oblique incidence angles (5°, 10° and 15°) using FDTD simulation (see section 3.3.1 and Figure 15). While we clearly observe the effect of off-axis aberrations, the extended depth of focus remains the same for different angles. We emphasize, however, that as the inverse design figure of merit did not explicitly handle nonzero incident angles, we do not expect such aberrations to be mitigated in our design. We fit the intensities near the focal plane using a Gaussian function to estimate the full-width-half-maxima (FWHM). Figs. 8G-O show the Gaussian fit focal spot at the center focal plane, and at two ends of the line along which the beam profile starts to become double Gaussian. We identified the depth of focus as the range along the optical axis, where the beam profile remains Gaussian. The minimum FWHM for fabricated EDOF metalenses with three different focal lengths (66.66 μm,100 μm,133.33 μm) which are shown in Figs. 8H, K, N are 1.07 μm, 1.7 μm, 2.32 μm, respectively. In Fig. 9 we plot the cross-sections of the focal plane of the EDOF and traditional metalens to compare the PSFs. Clearly the PSF for both lenses look similar, although the FWHM is slightly larger for the EDOF metalenses.

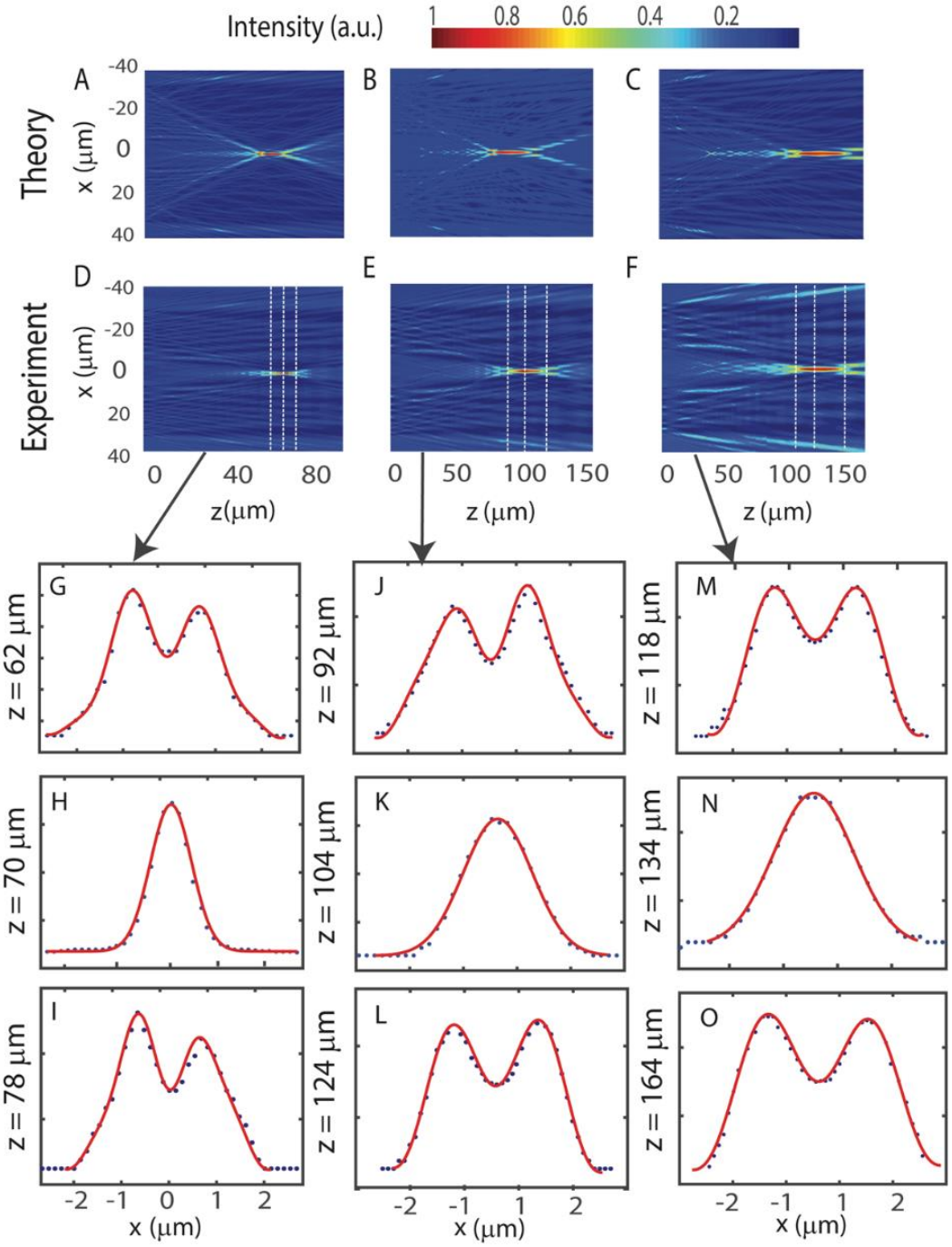

Figure 8: Simulated intensity along the optical axis of the designed EDOF metalenses with focal lengths of (A) 66.66 μm, (B) 100 μm, and (C) 133.33 μm. Experimentally measured field profile along optical axis for EDOF metalenses with focal lengths of (D) 66.66 μm, (E) 100 μm, and (F)

133.33 µm. (G-O) show cross-section of the beam size in different distance from the EDOF metalenses with a Gaussian and a double Gaussian fit.

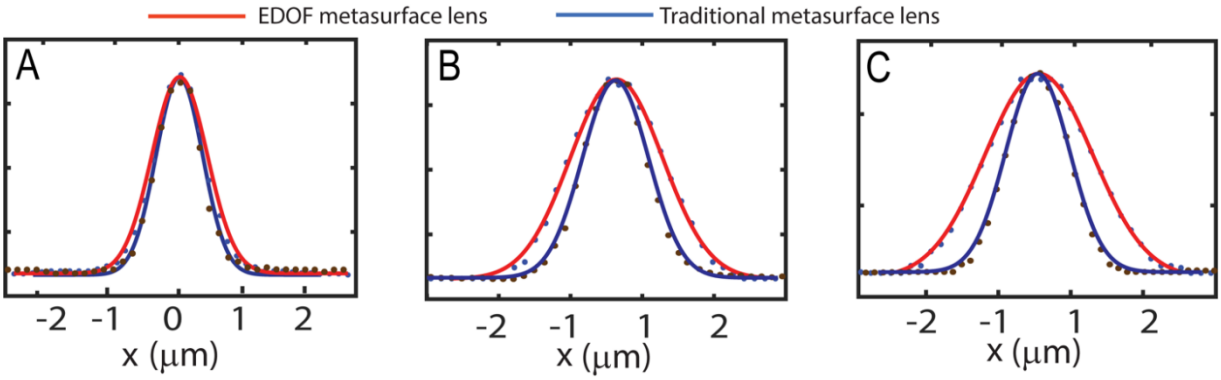

Figure 9: PSF of the traditional and EDOF metalenses for three different focal lengths: (A) 66.66 µm, (B) 100 µm, and (C) 133.33 µm.

By plotting the FWHM as a function of the distance along the optical axis, we estimated the focal length of the metalenses (Figs. 10A-C). We then estimated the focusing efficiency of the lenses along the optical axes. We define the focusing efficiency as the power within a circle with a radius of three times the FWHM at the focal plane to the total power incident upon the metalens. The FWHM at the focal plane is calculated as the minimum FWHM from the Figs. 10A-C. We plot the focusing efficiency of the metalenses along the optical axis (Figs. 10D-F). We expect the focusing efficiency to remain the same along the depth of the focus, and then drop off as we longitudinally move away from the depth of focus. Clearly, for the EDOF metalens, the efficiency remains high over a longer depth as expected. Table-3 summarizes the performance of all the metalenses, in terms of FWHM, focal length, efficiency, and depth of focus. We find a reasonable agreement between the simulation and experimental results. Additionally, we clearly observed an extended depth of focus in the inverse-designed metasurfaces compared to the ordinary metalenses. We note that, in simulation we sample along the optical axes more finely compared to

the experiment, which determines a larger error bar in experimentally measured depth of focus. We also observe no significant efficiency degradation between the ordinary metalenses and the EDOF metalenses. Other potential EDOF alternatives (e.g., axicons, log-aspheres, or cubic functions) also exist for 1D lenses; however, different regions of these lenses focus at different depths, significantly limiting the focusing efficiency. We designed and simulated these EDOF cylindrical lens metasurface alternatives to compare their performance with our inversed designed structure. To make a fair comparison with one of our lenses, other 1D EDOF lenses are designed to have central focal spot at 100 μm and a depth of focus of 30 μm (see the section 3.3.2 and Figure 16 for the simulated field intensity along the optical axis of these elements and corresponding PSFs). The focusing efficiencies of 1D log-asphere, axicon, and cubic lens were 12.16%, 8.6% and 14.47%, respectively. These efficiencies are significantly lower than that of our inverse designed EDOF lens.

We demonstrated inverse designed EDOF cylindrical metalenses for the first-time. While several theoretical designs exist for cylindrical EDOF lenses, to the best of our knowledge no experimentally demonstrated EDOF cylindrical lenses have been reported before. While we extended the depth by a factor of $\sim 1.5 - 2$, the depth of focus can be further extended albeit at the cost of reduced efficiency.

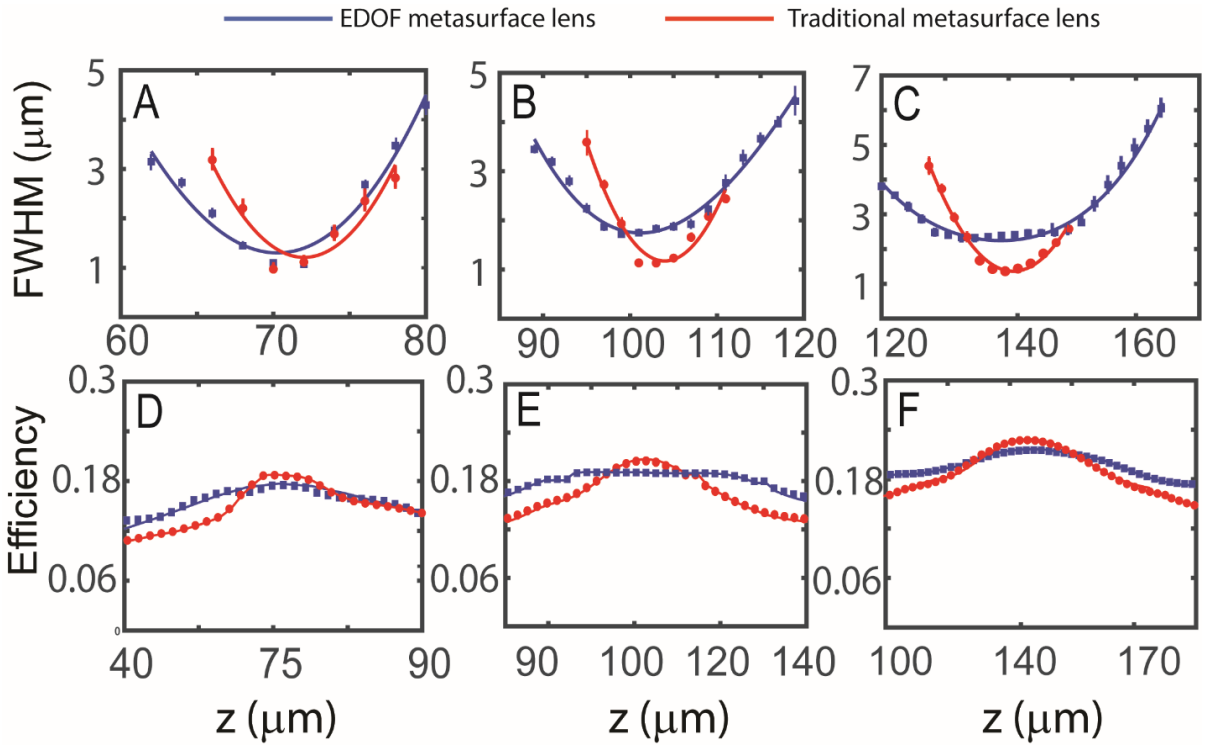

Figure 10: Performance of fabricated ordinary and EDOF metalenses as a function of distance along the optical axis. Measured FWHM of ordinary and EDOF metalenses as a function of distance corresponds to 66.66 μm (A), 100 μm (B), and 133.33 μm (C) metalenses. Measured focusing efficiency of 66.66 μm (D), 100 μm (E), and 133.33 μm (F) metalenses as a function of distance along the optical axis.

Table 3: Comparison between the ordinary and EDOF metalenses for 66.66μm, 100μm, 133.33μm metalenses, respectively

Lens Properties	**Ordinary Metalens**		**EDOF Metalens**	
	Simulation	**Experiment**	**Simulation**	**Experiment**
FWHM (μm)	**0.95**	**0.97**	**0.96**	**1.07**
	1.1	**1.13**	**1.3**	**1.7**
	1.2	**1.36**	**2.25**	**2.32**
Depth of Focus	$\mathbf{12}(\pm\mathbf{0.05})$	$\mathbf{12}(\pm\mathbf{2})$	$\mathbf{17}(\pm\mathbf{0.05})$	$\mathbf{16}(\pm\mathbf{2})$
(μm)	$\mathbf{14}(\pm\mathbf{0.05})$	$\mathbf{16}(\pm\mathbf{2})$	$\mathbf{30}(\pm\mathbf{0.05})$	$\mathbf{30}(\pm\mathbf{2})$
	$\mathbf{18}(\pm\mathbf{0.05})$	$\mathbf{22}(\pm\mathbf{2})$	$\mathbf{44}(\pm\mathbf{0.05})$	$\mathbf{44}(\pm\mathbf{2})$
Efficiency	**19.1**	**18.6**	**16.8**	**16.34**
(%)	**22.26**	**21**	**19.3**	**20.12**
	24.18	**24.65**	**22.21**	**23.48**
Focal Length	$\mathbf{67}(\pm\mathbf{0.05})$	$\mathbf{70}(\pm\mathbf{2})$	$\mathbf{64.2}(\pm\mathbf{0.05})$	$\mathbf{70}(\pm\mathbf{2})$
(μm)	$\mathbf{102}(\pm\mathbf{0.05})$	$\mathbf{102}(\pm\mathbf{2})$	$\mathbf{99.7}(\pm\mathbf{0.05})$	$\mathbf{104}(\pm\mathbf{2})$
	$\mathbf{136}(\pm\mathbf{0.05})$	$\mathbf{138}(\pm\mathbf{2})$	$\mathbf{129.8}(\pm\mathbf{0.05})$	$\mathbf{134}(\pm\mathbf{2})$

3.2 2D EDOF METALENSES

In the previous section we demonstrated inverse designed EDOF cylindrical metalenses for the first-time. We focused on 1D cylindrical lenses for the simplicity of design, cylindrical lenses are similar to spherical lenses in the sense that they converge or diverge light, but they have optical power in only one dimension and will not affect light in the perpendicular dimension. Consequently, they are not suitable for 2D imaging. Additionally, there are many other relevant factors for high-quality imaging including geometric aberrations, getting commensurate PSFs for different incident angles and good efficiency which are not specified in our figure of merit. However, we believe that the demonstrated inverse design method can incorporate a more complicated figure of merit to create a metasurface more suitable for imaging**.** In this section, we will be to extend our inverse design concept to 2D lenses and demonstrate imaging over a broader optical bandwidth than what is possible using a traditional metalens using a more complex figure of merit. Going beyond an extended depth of focus, the inverse design techniques can be used to engineer the PSF for other functionalities with potentially far-reaching impacts in computational imaging and microscopy.

3.2.1 *Introduction*

As we mentioned in the previous sections metalenses have been touted as a promising alternative to conventional, bulky refractive lenses. These metalenses, however, are diffractive and thus exhibit severe chromatic aberrations, limiting their utility and precluding their usage with incoherent, broadband white light. While refractive optical lenses also suffer from material dispersion, the resulting chromatic aberration is significantly lower compared to that of diffractive elements [58], including metalenses, where the severe chromaticity mainly comes from its fixed phase discontinuities at Fresnel zone boundaries [57].

In recent years, several approaches have been proposed to eliminate the chromatic aberrations of metalenses [59-60]. For example, multiplexing different unit cells designed for several discrete wavelengths can enable high-quality polychromatic metalenses [59-60]. In another design, multilayer metasurfaces capable of focusing discrete colors of red, green, and blue have been proposed to alleviate chromatic aberrations [60]. These polychromatic lenses, however, are not suitable for broadband white light imaging. Separately, there have been a number of broadband imaging demonstrations using dispersion engineering [61-65], which employs scatterers that compensate for both the group delay, and group delay dispersion. These broadband metalenses, however, have a constrained design space, limited to small lens aperture and low numerical aperture (NA) due to the limited group delay that is practically achievable with meta-atoms [66-67]. For example, in Ref. 62 [62] the reported achromatic metalenses have a diameter of $200\mu m$ ($\sim 100\mu m$) and a NA of 0.02 (0.106). Moreover, these dispersion-engineered meta-molecules generally entail multiple, coupled scatterers per unit cell, necessitating smaller features relative to standard metalenses, presenting challenges for high-throughput manufacturing [66, 68]. Another approach to mitigate chromatic aberrations is to employ meta-optics in conjunction with computational postprocessing [69-72]. While this method requires additional power and latency due to the computational reconstruction, using appropriately designed meta-optics, broadband images can be captured with large aperture and NA meta-optics, with possible lens diameters in mm-scale to cm-scale. The underlying idea is to extend the depth of focus of the meta-optics, such that all wavelengths reach the sensor in an identical fashion, i.e., the point spread function (PSF) at the sensor plane is wavelength invariant. By characterizing the PSF a priori, we can reconstruct the image from the captured sensor data via deconvolution. This hybrid meta-optical digital approach was first reported using a cubic phase mask (CPM) and Weiner deconvolution. A CPM

generates an Airy beam, which propagates through free space without significant distortion. While Airy beams over a broad range of wavelengths behave similarly, the PSF does not resemble that of a lens, which can introduce asymmetric artifacts in images when the signal-to-noise ratio (SNR) is low. Using rotationally symmetric extended depth of focus (EDOF) lenses, the image quality can be improved [73], as recently demonstrated by logarithmic-aspherical [74] and shifted-axicon meta-optics. However, the achievable optical bandwidth is still limited, as the PSF as a function of wavelength exhibits significant variation (as measured by its correlation coefficient [73]). Additionally, many of these EDOF lenses are designed such that segmented regions of the lens focus at different depths, which contributes to haze and a large DC component in the modulation transfer function (MTF).

In this section, we employ inverse design techniques to create an EDOF meta-optic with broad optical bandwidth while maintaining a lens-like PSF. Here, the design process starts from the desired functionality mathematically described by a figure of merit (FOM), and the scatterers are updated to optimize the FOM. Inverse design techniques have recently generated strong interest in nano-photonics and meta-optics and have been employed to design high efficiency periodic gratings [75, 76], monochromatic lenses [77, 78], PSF-engineered optics [79] and achromatic lenses [80-82] to name a few. In this work, we report a 2D EDOF meta-optics with four-orders of magnitude larger number of degrees of freedom and demonstrate full-color imaging over a broader optical bandwidth than what is possible using state-of-the-art EDOF metalenses. We show that the optical bandwidth in the inverse-designed meta-optic is 290nm in the visible wavelength range, at least a factor of 2 higher than that of existing EDOF metalenses. Unlike most existing implementations of diffractive or refractive EDOF lenses, the reported EDOF metalens

creates a lens-like PSF, without introducing significant blur and maintaining high focusing efficiency.

3.2.2 *Design*

We performed a large-scale optimization of meta-optics using the framework reported before [83] and extended to three-dimensional Maxwell's equations [84, 85]. Designing a large-area meta-optic with a brute-force solver is challenging, because meta-optics present two very different length scales: a macro scale (~mm diameter of the whole optic) and a nano scale (the smaller features of the scatterers) which are difficult to resolve concomitantly [86]. To overcome this limit and significantly accelerate the simulation and optimization problems, we use a hybrid multi-scale photonic solver, which relies on a locally periodic approximation [87] where the nanoscale is approximated by a surrogate model, and the macroscale is solved by a convolution with the analytical free space Green's function [83]. In the present work, we fit a surrogate model that quickly evaluates the complex transmission of a unit cell as a function of its parameter change using Chebyshev interpolation [88]. We considered two parameterizations of the unit-cell geometry with a period of 400 nm: for the 100-μm-focal-length meta-optic, a cylindrical pillar of silicon nitride (SiN) on top of silica with a diameter varying from 100 nm to 300 nm (considering a minimum fabricable feature of 100 nm); for the 1-mm-focal-length meta-optic, a square nanofin of SiN on top of silica with each side of the nanofin varying from 100 to 300 nm. When the number of parameters for the scatterer is greater than five, Chebyshev interpolation suffers the "curse of dimensionality", and a neural network surrogate becomes preferable [89]. The figure of merit to be maximized is the minimum intensity along the focal axis and the depth of field was designed for an incident plane wave at 633 nm. We found that a spacing of 1.2 μm between two evaluations of intensity along the optical axis is optimal to result in a flat intensity profile over the desired

depth of field. Consequently, in contrast to the depth of focus of a traditional lens, which depends on the ratio between focal length of the device and its diameter, the number of intensity evaluations for the EDOF minimax problem is proportional to the diameter of the device. For the 100-μm-focal-length meta-optic, we maximized the minimum intensity over 65 evaluations between a depth of 75 μm and 150 μm. For the 1-mm-focal-length meta-optic, we maximized the minimum intensity over 422 evaluations between a depth of 0.75 mm and 1.25 mm. Note that the latter optimization is 6.5 times more constrained than the former, therefore resulting in a poorer optimum. To ensure polarization insensitivity, the designed meta-optic has C4v symmetry. We also designed two traditional metalenses with the same focal lengths of the inverse-designed ones using traditional forward design method. This forward design technique is based on rigorous coupled-wave analysis (RCWA) and finite-difference time-domain (FDTD) simulation. In the forward design method, we arrange the scatterers on a subwavelength lattice, and spatially vary their dimensions based on the spatial phase profile of a hyperboloid metalens. We note that the reported meta-optics is one of the largest inverse-designed nanophotonic structure reported in the literature.

To validate our design, we fabricated both the inverse-designed EDOF meta-optics and forward-designed traditional hyperboloid metalens. The diameter for these metalenses is 1mm and 100 μm. The EDOF and traditional metalenses are fabricated in silicon nitride on the same sample. We first deposited 600-nm-thick layer of silicon nitride using Plasma-enhanced chemical vapor deposition (PECVD) on a 500- μm -thick fused-silica. The sample was spun coated with a layer of 200-nm-thick positive electron beam resist (ZEP-520A), followed by an additional layer of conductive material (Au/Pd) to avoid charging effects during electron beam lithography. After that, the pattern is written using electron-beam lithography (JEOL JBX6300FS at 100 kV), and the

exposed sample was developed in amyl acetate. Next, around 50-nm-thick aluminum was evaporated directly onto the developed sample. After performing lift-off, the silicon nitride layer is etched through its thickness using an inductively coupled plasma etcher with a mixture of CHF3 and O2 gases. In the end, the remaining aluminum was removed in AD-10 photoresist developer.

Figs. 11A-B show the scanning electron micrographs (SEMs) of the fabricated inverse-designed EDOF meta-optics and a zoom-in SEM showing the silicon nitride nano pillars forming the circularly symmetric EDOF meta-optics. A custom microscope setup (see section 3.3.3 and Figure 17) under illumination by a 625 nm light-emitting diode (part number Thorlabs-M625F2) is used to measure the depth of focus of our fabricated meta-optics. Figs. 11C-F show the experimentally measured intensity profiles along the optical axis for the two traditional metalenses and two inverse-designed EDOF meta-optics. The intensity profiles along the optical axis are captured using a camera and translating the microscope along the optical axis using an automated translation stage with an axial resolution of 1 μm (Figs. 11C, E) and 2 μm (Figs. 11D, F). We clearly observe an elongation of the focal spot along the optical axis. We identified the depth of focus as the range along the optical axis, where the beam profile remains Gaussian. We measured the depth of focus to be ~83 μm (~0.4 mm) for our 100 μm (1 mm) EDOF meta-optics. The depth of focus is only 10 μm (0.1mm) for the 100 μm (1mm) aperture traditional metalens. We also measured the focusing efficiency of the 1 mm aperture lenses along the optical axes (see section 3.3.4 and Figure 18). We did not observe significant degradation of the efficiency in the designed EDOF optics (efficiency of 47%) compared to the traditional metalens (efficiency of 51%).

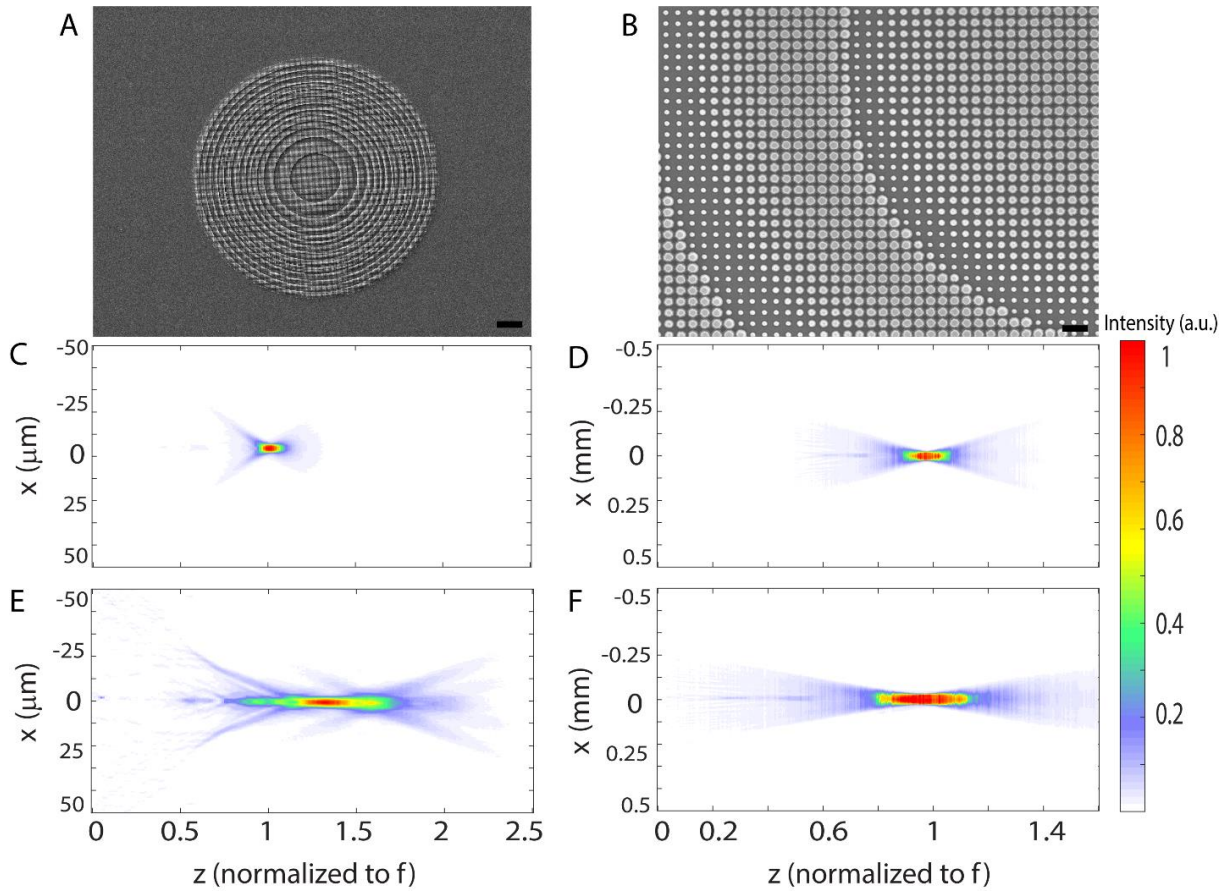

Figure 11. Scanning electron micrograph (SEM) of (A) inverse-designed EDOF meta-optics, (B) Zoom-in SEM on inverse-designed EDOF meta-optics showing silicon nitride scatterers forming the EDOF metalens; The scale bars correspond to 10 μm (A) and 1 μm (B), (C-F) Experimentally measured field profile along optical axis for traditional (C, D) and inverse-designed EDOF metalenses (E, F) with focal lengths of (C, E) $f = 100$ μm, (D, F) $f = 1$ mm.

Fig. 12A. shows the cross-sections of the focal plane of the 1 mm and 100 μm aperture inverse designed EDOF and 1 mm traditional metalens to compare the PSFs. We also fit the intensities near the focal plane using a Gaussian function to estimate the full width at half maximum (FWHM) of the beam profiles. The minimum FWHM for the fabricated EDOF meta-optics and traditional metalens with 1 mm (100 μm) aperture focal length is 24.9 μm (3.35 μm)

and 20.6 μm (3μm), respectively as shown in Fig. 12A. The diffraction-limited spot of our 1mm aperture metalens with the same geometric parameters is 1.46 μm. We note that, in this work, the diffraction limited FWHM for a lens is calculated by fitting a Gaussian function to the Airy disk with the same geometric parameters. The difference between the diffraction limit and the experimentally measured FWHM comes from the geometric aberration. This aberration is expected to scale linearly with the aperture [90]. This is why the FWHM for 1mm lens is almost ~10 times larger than that of the 100μm lens, even though both aperture lenses have the same NA. We note that, these aberrations could be further minimized by redefining the FOM in the inverse design.

Nevertheless, the PSF for both EDOF and traditional lenses are quite similar, unlike traditional EDOF lenses. The PSF of our EDOF metalens, however, remains identical over an extended distance along the optical axis, making the PSF insensitive to focal shift, e.g., due to the wavelength change. This property enables the EDOF meta-optics to produce similar PSFs for all wavelengths at one specific plane. On the other hand, the PSF of a standard metalens varies significantly with wavelength. To quantitatively understand this behavior, the MTF is calculated for our EDOF and a traditional metalens as shown in Figs. 12C, D. The MTF of a traditional lens measured at the focal plane for 530 nm preserves more spatial frequency information for green light (530 nm) compared to red (625 nm) and blue (455 nm). On the other hand, the MTF for our EDOF meta-optics remains same for all three colors. In fact, not just these three colors, the MTF of the EDOF meta-optics remains same over the whole visible range. Additionally, the EDOF meta-optics also exhibits a higher cutoff frequency than a traditional metalens.

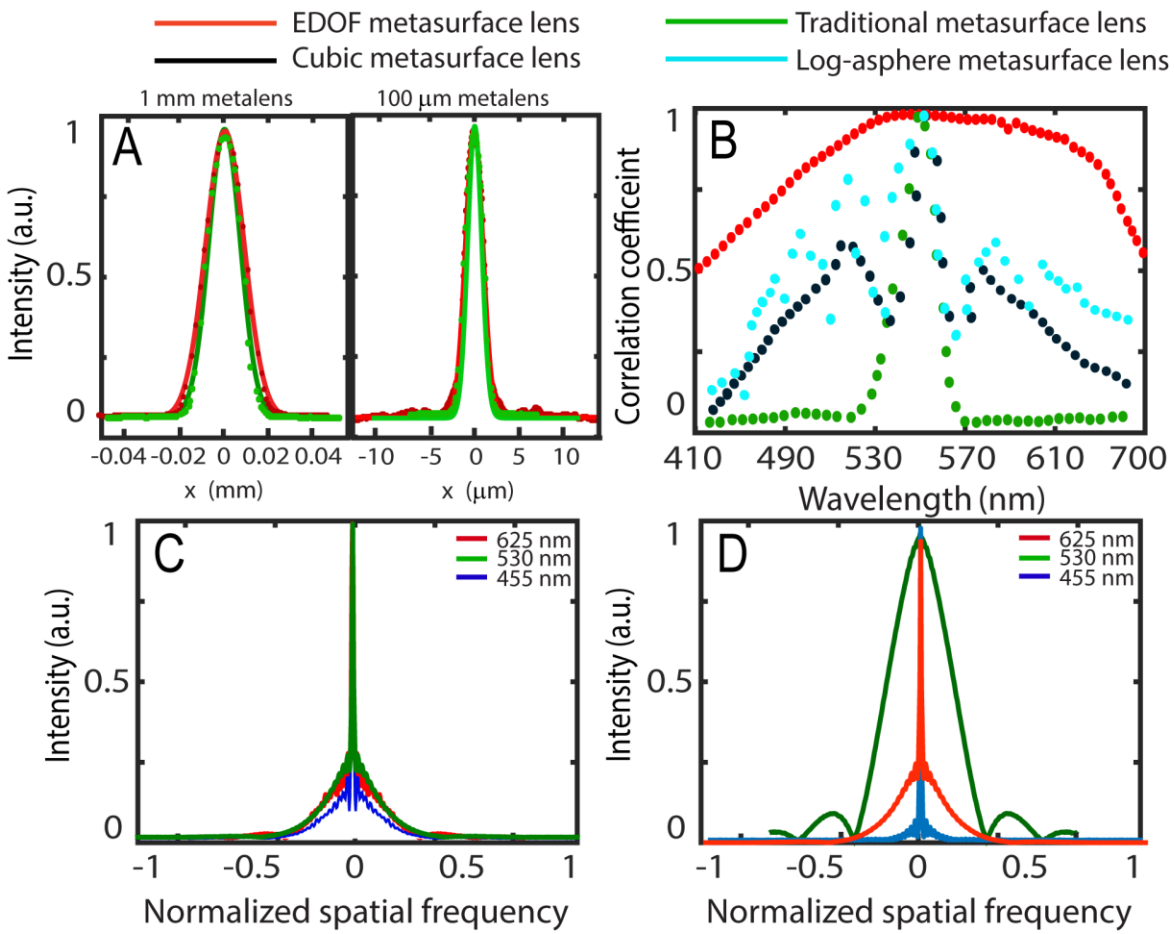

Figure 12. Characterization of the metasurfaces: (A) PSF of the traditional and EDOF metalenses for 1mm and 100 μm focal length. (B) Correlation coefficient plots for four different metalenses as a function of wavelength. (C-D) The corresponding x–y plane cross sections of the experimental MTFs for our EDOF metalens (C) and traditional metalens (D) are displayed with red lines from its PSF measured under red light, green lines under green light, and blue lines under blue light. The MTF plots have a spatial frequency normalized to 560 cycles/mm.

Having a highly wavelength-invariant MTF across a large optical bandwidth is necessary for applying computationally efficient deconvolution techniques to recover high-quality, full-color images. One metric for quantifying this invariant behavior is to calculate the correlation between

PSFs. The correlation can be calculated as the inner product between a reference PSF (here we used the PSF at 530 nm) and the PSFs at all other wavelengths in the range of interest. To compare the performance of our inverse designed EDOF metalens with other existing EDOF metalenses, we also calculate the correlation coefficients of log-asphere and cubic metalenses (Fig. 12B). To make a fair comparison, all these meta-optics are designed at 530 nm wavelength. Fig. 12B clearly shows that the correlation coefficient of our inverse designed EDOF is higher and far more uniform compared to other metalenses over a broad wavelength range. We defined the optical bandwidth as the range of optical wavelengths where this correlation coefficient is greater than 0.5. We estimated the optical bandwidths relative to a central wavelength (530 nm) to be 290 nm (inverse-designed EDOF), 130 nm (log-asphere metalens), 95 nm (cubic metalens), and15 nm for a standard metalens. We also calculated the fundamental limit on the achievable optical bandwidth based on the given thickness and numerical aperture of our meta-optics [91]. This fundamental limit is only ~20 nm for a hyperboloid metalens, consistent with our experimental results and significantly lower than that achieved with our EDOF designs.

3.2.3 *Imaging Results*

A larger aperture lens collects more photons and thus can capture images with higher SNR. Consequently, we focus on 1 mm EDOF meta-optics for imaging. The captured image in our system can be written in the form of $f = Kx + n$ [44], where K is the system kernel or PSF, x is the desired image, and n is the noise that corrupts the captured image f. While there are several methods to estimate the image x, we chose to use Wiener and total variation (TV)-regularized deconvolution due to their effectiveness and generalizability to different scenes relative to deep learning-based deconvolution methods.

Our system kernel is sampled by measuring PSFs for our EDOF metalens at three wavelengths using separate LED sources centered at 625 nm, 530 nm and 455 nm (Thorlabs M625F2, M530F2, M455F1). To demonstrate the imaging capability of our EDOF system, we first considered narrowband LED imaging (bandwidth ~20nm) for three different wavelengths. Fig. 13 shows our EDOF imaging performance compared to a traditional metalens with and without deconvolution. Although our original image is focused for red light as shown in Fig. 13A, the images captured under green and blue light (Fig. 13B, C) are severely distorted due to strongly defocused PSFs in these wavelengths. On the other hand, the images which are captured by inverse-designed EDOF metalens under green and blue illumination (even before deconvolution) are less blurry compared to those of a standard metalens, thanks to their symmetric and wavelength-invariant PSFs. After deconvolution, the captured images appear even sharper and in focus for all wavelengths. We noticed that our image under blue light illumination is not as focused as red and green. Although our figure of merit includes the blue wavelength in the inverse design method, we attribute the lower image quality for blue to its PSF correlation coefficient being lower compared to other part of the visible regime. To quantitatively estimate the imaging quality, we calculated the structural similarity index measure (SSIM) [93] for the captured images in Fig. 13. The calculated SSIMs between the original image and the output images from EDOF (traditional) metalenses are 0.637 (0.492) for the red channel, 0.503 (0.239) for the green channel, and 0.363 (0.149) for the blue channel. Thus, for all the wavelengths, our EDOF metalens provides a higher SSIM than that of the conventional metalens. In addition to Wiener deconvolution algorithm, we used TV-regularization for image denoising and deconvolution. TV regularization is based on the statistical fact that natural images are locally smooth, and the pixel intensity gradually varies in most regions.

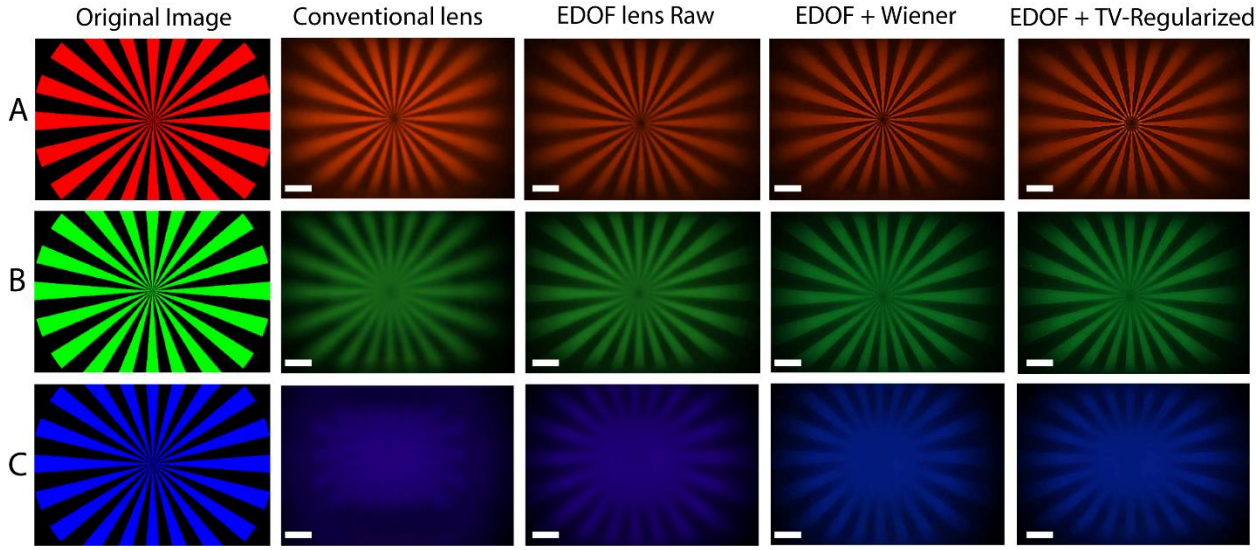

Figure 13. Imaging at discrete wavelengths. The appropriately cropped original object patterns used for imaging are shown in left side of the figure. Images were captured with the singlet traditional metalens, the EDOF lens without, and with deconvolution (EDOF + Wiener), and with the total variation (TV) regularization. Images were captured using narrowband (bandwidth of 20nm) LEDs with center wavelengths at (A) 625 nm, (B) 530 nm and (C) 455 nm wavelength. The scale bars correspond to 100 μm.

Finally, our EDOF system was tested with a full-color OLED display (SmallHD 5.5 in). The OLED monitor was placed ~13 cm away from our EDOF metalens, which displays some of our ground-truth images as shown in the Fig. 14. The images were chosen in a way to have all the combination of visible colors. The chromatic aberration is clearly observed on captured images with a conventional metalens. However, the raw images which are captured by the EDOF metalens show less chromatic aberration, even though they are still blurred before deconvolution. We then computationally processed the captured images using Wiener deconvolution and TV regularization algorithm. The post processed images show in focus, smooth and less aberrated images. We note

that such deconvolution cannot mitigate the chromatic aberration in the conventional metalens as the MTFs outside green wavelength is too distorted. We also noticed that, for the case of colorful floating balloons (Fig. 14D), the chromatic blur for blue balloons is still there, due to the low PSF correlation coefficient in this wavelength as explained earlier. Nevertheless, the achromatic performance of the inverse-designed meta-lens is significantly better than that of the metalens. We note that due to the narrow MTF of the metalens over a broad wavelength range, any deconvolution operation on the post-capture images significantly amplifies the noise, making the reconstructed images significantly worse than the captured ones. Hence, we only report the captured data for a metalens, and no reconstructed images are shown here.

We also characterized the imaging quality of our inverse designed EDOF meta-optics compared to other existing EDOF metalenses such as cubic or log-aspheres, by calculating the SSIM for “ROYGBVWG” image (see section 3.3.5, Figure 19 and Table 4). The calculated SSIMs between the original image and the output images from inverse designed EDOF metalenses are higher than the SSIM values from other EDOF lenses (see, Table. 4). Thus, our inverse designed EDOF metalens indeed provide a higher SSIM score and better imaging quality than other existing EDOF lenses. This already shows the benefit of inverse design, which can be further improved by considering angle-dependence of the scatterers and other aberrations in the FOM.

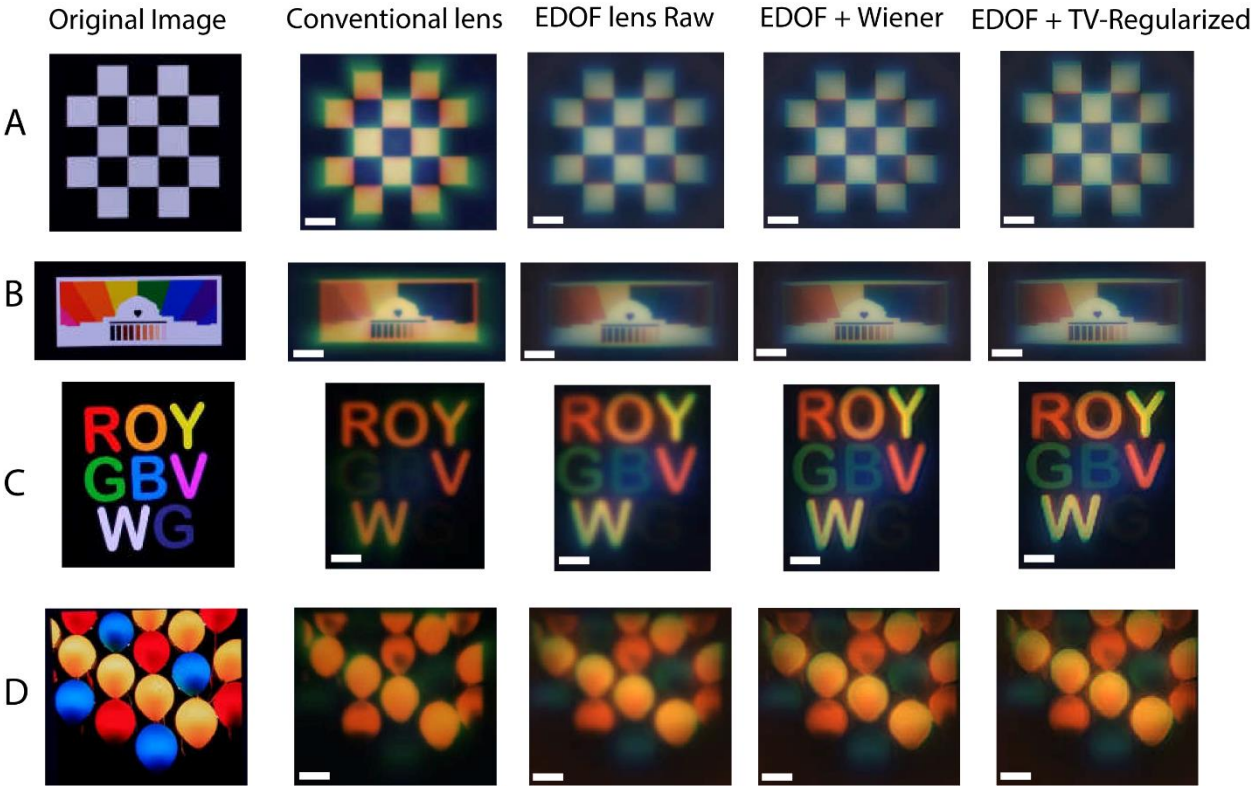

Figure 14. White light imaging. Images were taken from an OLED display of (A) white-black cross pattern, (B) colored rainbow MIT pattern, (C) colored letters in ROYGBVWG and (D) colorful floating balloons. The appropriately cropped original object patterns used for imaging are shown in the left column. The scale bars correspond to 100 μm.

3.2.4 *Discussion*

Using an inverse design method, for the first time, we created a 2D EDOF metalens that has a symmetric PSF, large spectral bandwidth, and that also maintains focusing efficiency comparable to that of a traditional metalens. The proposed inverse designed EDOF meta-optics in conjunction with computational imaging is used to mitigate the chromatic aberrations of traditional metalenses. Unlike other existing EDOF metalenses (log-asphere lenses or other variants), our inverse-designed EDOF metalens represents a highly invariant PSF across a large spectral bandwidth to improve the full-color image quality. We have quantified this via calculating and comparing the PSF correlation coefficient with other EDOF metalenses over the visible spectral range. We emphasize that this is the largest aperture (1 mm) meta-optics ever reported for achromatic imaging, and as such there is no fundamental limitation on increasing aperture, like dispersion engineered meta-optics do.

While we extended the spectral bandwidth and demonstrated achromatic imaging even without post processing algorithms, our images still need to be computationally processed to give us in-focus and better-quality images. This postprocessing adds latency and power to the imaging system. Additionally, we have primarily focused on chromatic aberration corrections, and Seidel aberrations are largely ignored. Using a more involved figure of merit and including the angular dependence, a longer depth of focus metalens can be designed, which can potentially preclude the use of computational postprocessing. In this work, we also emphasize the utility of rotationally symmetric EDOF metalenses (for simplified packaging and mitigating deconvolution artifacts), as well as larger apertures (1 mm) compared to our previous works. A larger aperture will enable more light collection, higher signal-to-noise ratio and faster shutter speed, which are crucial for practical applications. We envision that the image quality can be further improved by co-designing

the meta-optics and computational back end [94, 95], as has already been reported to provide very high-quality imaging [94].

3.3 Material and Methods

3.3.1 *Comparison with other potential EDOF lenses*

Other potential EDOF alternatives (e.g., axicons, log-aspheres, or cubic functions) also exist for 1D lenses; however, different regions of these lenses focus at different depths, significantly limiting the focusing efficiency. We designed and simulated these EDOF cylindrical lenses via the forward design method. The forward design method of these metalenses involves selecting the appropriate spatial phase profile (e.g., axicons, log-aspheres, or cubic functions) for the specific optical component, arranging the scatterers on a subwavelength lattice, and spatially varying their dimensions. To make a fair comparison with one of our inverse-designed lenses, other 1D EDOF lenses are designed to have central focal spot at 100 μm and a depth of focus of 30 μm. The field intensity profiles of these EDOF lenses are simulated using 2D finite-difference time-domain (FDTD) simulation with an axial sampling resolution of 50 nm (Figure 15). The focusing efficiencies of 1D log-asphere, axicon, and cubic lens were 12.16%, 8.6% and 14.47%, respectively. Even though, these 1D EDOF lenses can also provide an EDOF, their efficiency is significantly lower than that of our design, which is 20.12%. In this paper, the focusing efficiency is defined as the power within a circle with a radius of three times the FWHM at the focal plane to the total power incident upon the metalens Since FWHM, however, is not well defined for cubic lenses, we also calculated the focusing efficiency for this EDOF lens by taking the ratio of the intensity integrated within the aperture area of the device at the focal plane to that at the plane of

metalens instead of a circle with a radius of three times the FWHM. Using this definition, we got 67% focusing efficiency for EDOF 1D cubic lens.

In addition of focusing efficiency, The FWHM of these 1D log-asphere, axicon and cubic lenses are 1.75μm, 1.25μm and 1.7μm, respectively which are calculated using their corresponding Gaussian fit at the cross sections of the focal planes. These FWHM are comparable to our inverse-designed metalens. Thus, our inverse design approach produces a metalens with comparable FWHM of other existing EDOF lenses but maintains a higher focusing efficiency.

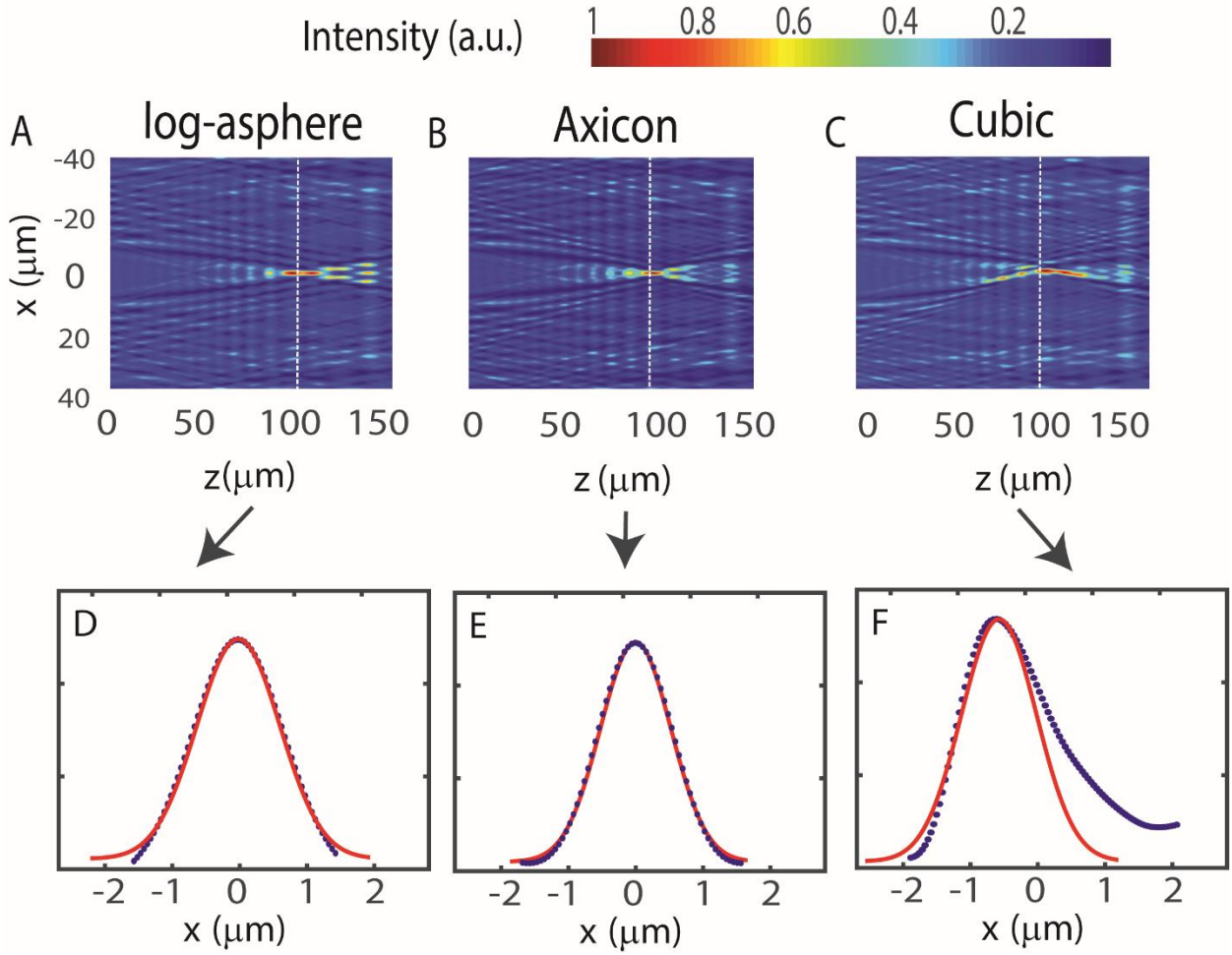

Figure 15: Simulated field intensity along the optical axis of alternative EDOF lenses with a focal length of 100 μm and depth of focus of 30 μm. We simulated intensity profiles for a log-asphere

(A), axicon (B), and a cubic phase mask (C). (D-F) Cross sections at the focal plane of these EDOF lenses with a corresponding Gaussian fit. The focusing efficiency of 1D log-asphere, axicon and cubic lenses were calculated using these cross sections are 12.16%, 8.6% and 14.47%, respectively.

3.3.2 *Simulated performance under oblique incidence*

In order to see how sensitive our inverse-designed EDOF lenses are to different incident angles, we also characterized the performance of the inverse-designed EDOF metalens under oblique incidence angles (5°, 10° and 15°) using FDTD simulation (Figure 16). While we clearly observe the effect of off-axis aberrations, the extended depth of focus remains the same for different angles. We emphasize, however, that as the inverse design figure of merit did not explicitly handle nonzero incident angles, we do not expect such aberrations to be mitigated in our design.

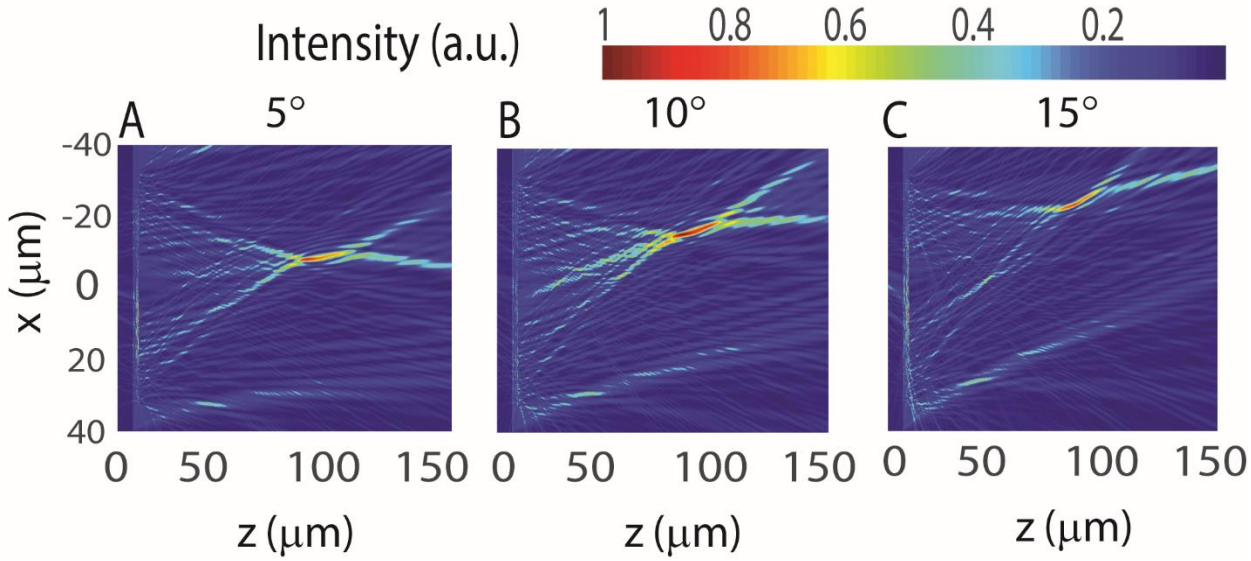

Figure 16: Simulated normalized field profile intensity of our inverse designed EDOF metalens with a focal length of 100 μm under oblique incidence. FDTD simulations were run for incidence angles of (A) 5 °, (B) 10 °, (C) 15 °. While we clearly observe the effect of off-axis aberrations in our simulation, there is a notable extension of depth of focus for different angles.

3.3.3 *Confocal microscopy setup*

A confocal microscopy setup under illumination by a 625 nm light-emitting diode (part number Thorlabs-M625F2) is used to measure extension of depth of focus for our fabricated metalenses. Fig. 17. shows the confocal microscopy setup that we have used to experimentally measured field profiles along the optical axis for the two traditional metalenses and two inverse-designed EDOF metalenses.

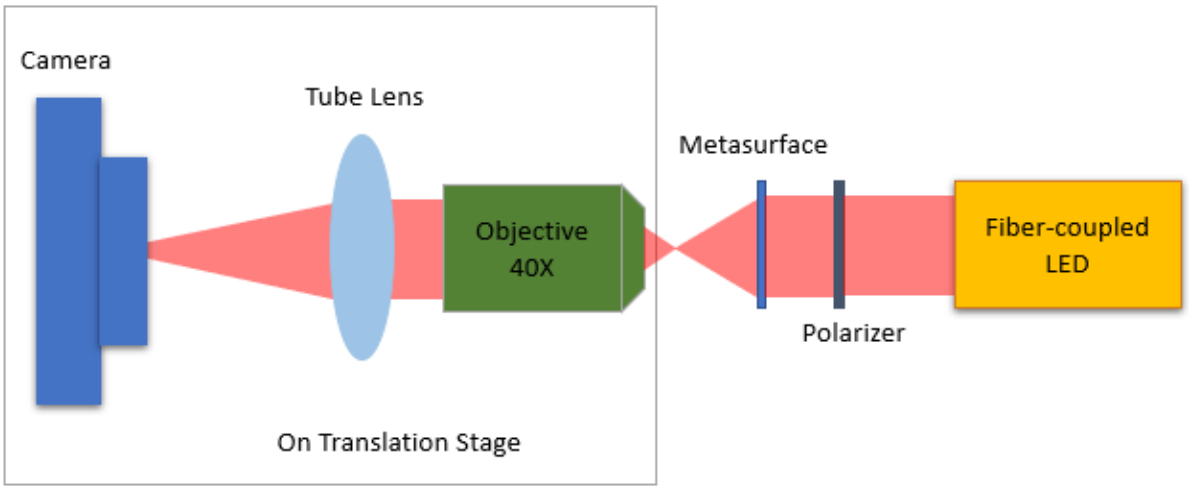

Figure 17. Confocal microscopy setup used to measure the metalenses.

3.3.4 *Experimental performance of the EDOF metalens*

We define the focusing efficiency as the power within a circle with a radius of three times the minimum full-width half maxima (FWHM) at the focal plane to the total power incident upon the metalens. We plot the focusing efficiency of the metalenses along the optical axis (Fig. 18). We expect the focusing efficiency to remain the same along the depth of the focus (for our EDOF metalens), and then drop off as we longitudinally move away from the depth of focus. Clearly, for the EDOF metalens, the efficiency remains high over a longer depth as expected. We did not observe significant degradation of the efficiency in the designed EDOF lenses compared to that of an ordinary lens.

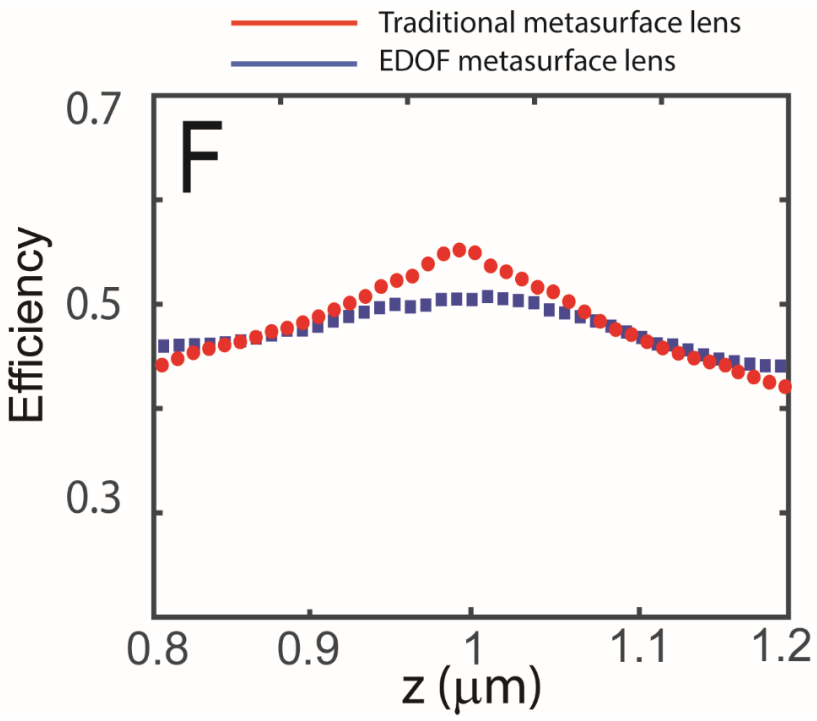

Figure 18. Experimentally Measured focusing efficiency of 1mm EDOF and traditional metalenses as a function of distance along the optical axis.

3.3.5 *Comparison with other potential EDOF lenses in terms of SSIM and imaging quality*

In order to see how imaging results of our inverse-designed EDOF lens outperform the standard and other potential EDOF lenses, we also characterized the imaging quality of our inverse designed EDOF metalens compared to other existing EDOF metalenses such as cubic functions or log-aspheres, by calculating the SSIM for "ROYGBVWG" image. The SSIM calculations are sensitive to the subject's translation, scaling, and rotation, which are difficult to eliminate in an experimental setup. Hence, we utilize the simulated PSFs and phase functions (cubic functions and log-aspheres) with the same geometric parameters to perform imaging and post processing for our "ROYGBVWG" image as it is shown in Fig. 19. The calculated SSIMs between the original image and the output images from inverse designed EDOF, conventional, cubic and log-asphere metalenses are shown in Table. 4. for the red, green, and blue channel. Clearly, our inverse designed EDOF metalens provides a higher SSIM score and better imaging quality than other existing EDOF lenses.

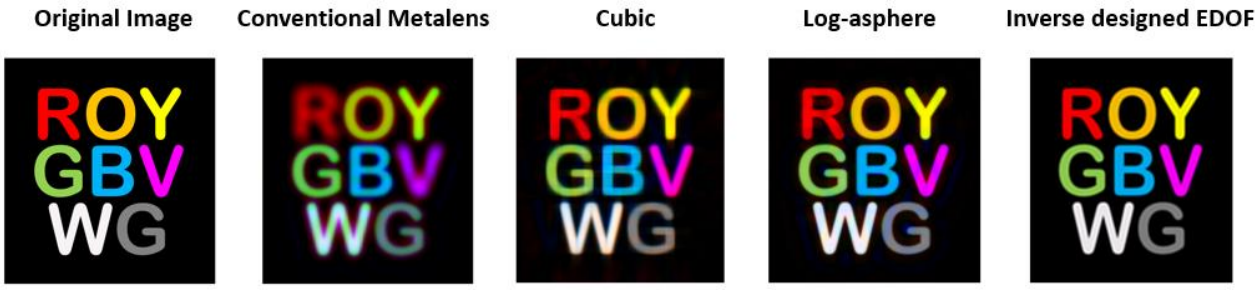

Figure 19. Simulated imaging performance after deconvolution. Deconvolved images captured by the EDOF imaging system, using the simulated images and PSFs.

Table 4. SSIM on Simulation-Restored Images for standard and different EDOF metalenses

Color channel	Inverse designed EDOF	Conventional Metalens	Cubic Metalens	Log-asphere Metalens
Red	**0.639**	**0.292**	**0.3062**	**0.4537**
Green	**0.7903**	**0.4691**	**0.6543**	**0.7170**
Blue	**0.4863**	**0.3449**	**0.4776**	**0.5718**

Chapter 4. AR METASURFACE SYSTEM

4.1 INTRODUCTION

Augmented reality (AR) technology has recently attracted considerable attention and could revolutionize technologies ranging from applications in the military and navigation, to education and entertainment. Using these devices, we can effectively integrate computer-generated virtual information into the real world. AR can be implemented in various ways, including smartphone displays, head-up displays (HUDs), and head-mounted displays (HMDs) [96]. Among the various approaches, see-through head-mounted near-eye displays (AR glasses) have been of primary focus because of their potential to provide an extremely high sense of immersion. One of the most vital components in a head-mounted display (HMD) is a near-eye visor (NEV). Current implementations of NEVs can be broadly classified into two categories: **reflection-based**, where light from a display placed near the eye is reflected off a freeform visor to enter the eye [97-98]; and **waveguide-based**, where light is passed through a waveguide and projected to the eyes using a grating [99-101]. While reflective visors can provide higher efficiency and transparency, they are often bulky and suffer from a small eye-box, and in general need to be placed far away from the eyes to achieve a wide field of view (FOV). Waveguide-based NEVs can provide a much more compact form-factor with sufficient eye-box expansion, although they often have lower FOV and efficiency. They also suffer from strong chromatic aberrations in both the image passed through the waveguide as well as in see-through mode as the gratings are diffractive in nature. The core of a waveguide NEV consists of the input and output couplers. These can be either simple prisms, micro-prism arrays, embedded mirror arrays [102], surface relief gratings [103], thin or thick

holographic optical elements (HOEs) [101], or diffractive optical elements (DOEs) [100]. The out-coupling efficiency of the gratings is, however, low, making the energy-efficiency of these waveguide-based visors poor relative to reflection-based visors. A closer look at reflective visors reveals that the trade-off between size and FOV of the NEV primarily originates from the fact that current NEVs rely on geometric reflections and refractions to bend light.

Unlike conventional diffractive optics, the subwavelength scatterers in a metasurface preclude higher-order diffraction, resulting in higher efficiency as all the light can be funneled into the zeroth order [104]. As diffraction can bend light by an angle more than reflection and refraction, it is possible to bring a metasurface closer to the eye, while maintaining a wide FOV. Recently, the first silicon metasurface freeform visor was designed by our group [105], providing a large field of view for virtual reality (VR) applications (77.3° both horizontally and vertically) when placed only 2.5 *cm* away from the eye. This metasurface visor, however, severely distorts the real-world view, has strong chromatic aberrations and is not transparent for AR applications. In addition to our group, several other metasurface-based visor designs have been reported in the literature for achieving large FOV, lighter designs and better see-through quality, including designs based on combinations of a metalens and dichroic mirrors [106-107], Pancharatnam-Berry phase metalenses [108], and a compact light engine based on multilayers-metasurface optics [109].

In this chapter, we propose a metasurface freeform optics-based NEV, that will circumvent real-world distortions and eliminate chromatic aberrations, as needed for an immersive AR experience. For this purpose, we propose to use a composite metasurface: one of the metasurfaces reflects light from the display to project the virtual world to the user's eye while the second metasurface circumvents the distortion of the real-world due to the first metasurface. The first metasurface is designed to have multi-chrome operation, which two metasurface together

preserves the color information in transmission. The resultant display FOV of the composite metasurface NEV is more than 77° both horizontally and vertically which is better than current existing AR visors and also it has acceptable see-through quality over the visible range (less than a wavelength RMS wavefront error).

4.2 THEORY AND DESIGN

First, we design and model the single metasurface NEV that can guide light from a display at the HMD to the human eye via ray optical simulation (ZEMAX-OpticStudio). The size of the visor is assumed to be $4\,cm \times 4\,cm$ to maintain a compact form-factor comparable to that of ordinary sunglasses while still having a large field of view when placed only 2.5 cm away from the eyes. The display is placed between the visor and the eye: 1cm away and 1.5 cm upwards from the visor with an angle of 45° with respect to the optical axis. The display is initially assumed to be monochromatic (540 nm). The eye model which we use here for simulation is the widely accepted model proposed by Liou & Brennan [110]. Here, it is assumed that the eye is looking out through an optical system, so the retina is the image surface. We model the visor phase-mask with Zernike standard polynomials [111]. We find that the first 6 Zernike terms converge in a reasonable time and are sufficient to guide light from the display to the human eye in an acceptable manner. A schematic of a ray tracing simulation from our reflective metasurface is shown in Fig. 20A. The first metasurface (near the eye) will be partially reflective, and the design principle will follow the ray tracing approach of sending light from each point on the display to the eye. The virtual display FOV from our simulation is estimated to be 77.3° along both vertical and horizontal directions. Fig. 20B illustrates the reflective phase-mask obtained from the Zernike standard polynomials from the first metasurface of our visor.

After designing the single metasurface near-eye visor, we design a pair of metasurfaces, where the second metasurface (located further from the eye) corrects any distortion of the real-world scene caused by the first metasurface. The gap size between two metasurfaces is assumed to be 500 μm which is fixed to facilitate future fabrication on both sides of a glass wafer. The corrective phase-mask of the second metasurface is also designed using Zernike standard polynomials. This phase mask is designed to minimize the RMS wavefront error [112] for light transmitted through two metasurfaces to ensure good see-through quality. Without using the corrective phase-mask the RMS wavefront error for light on the retina after passing through both metasurfaces is 14.8λ. Such wavefront errors represent the see through-quality, and with greater than wavelength rms error leads to a highly distorted view. However, after using the second metasurface to correct the distortion from the first metasurface, the RMS wavefront error is reduced to 0.9λ. We also calculated the RMS wavefront error of a freeform visor developed in [113] to compare to our see-through quality. The RMS wavefront error of the freeform visor is 1.17λ, which is better than a single metasurface but worse than our corrected composite metasurface visor.

Fig. 20 shows the optimized metasurface NEV phase profiles, where the first metasurface (Fig. 20B) distorts the light field, but in conjunction with the second metasurface (Fig. 20C), the optical wavefront error is minimized. Once the phase-functions are optimized, we implement them using metasurfaces, which is explained in more detail later in the paper.

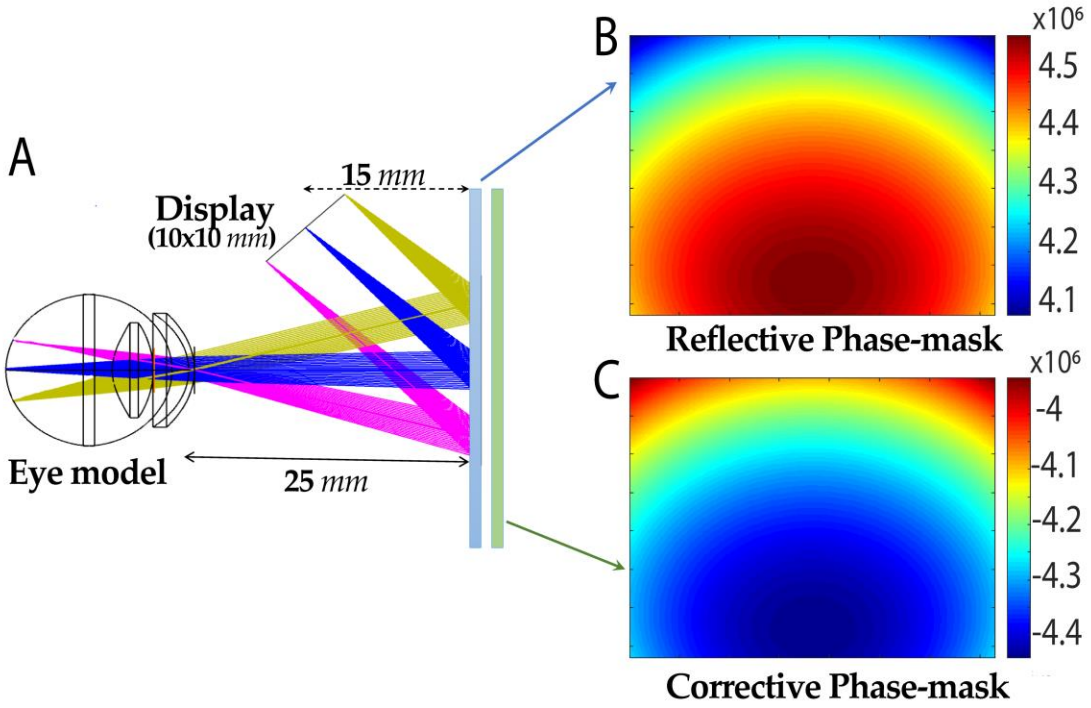

Figure 20. Metaform Visor (A) Schematics of metasurface NEV and its ray tracing simulation in ZEMAX. (B) Reflective phase-mask from first metasurface of our visor. (C) Corrective phase-mask for second metasurface of our visor. The size of the visor is assumed to be 4 cm×4 cm.

We also evaluate the modulation transfer function (MTF) and the grid distortion cause by the NEV to estimate the image quality. The MTF of the system along the tangential and sagittal plane is shown in Fig. 21A., exhibiting a value greater than 0.3 at 33 cycles/mm, which is a sufficient resolution for a human visual system and satisfying the Nyquist resolution for a 15μm pixel size. The grid distortion is less than 5.9% which is sufficient for human intelligibility (Fig. 21B.). Additionally, we simulate an image of the green crossbars (based on our operating wavelength design) in Zemax to evaluate the see-through quality before and after using the second phase-mask, as shown in Fig. 21C. The projected image of the crossbars is shown in the right side of Fig. 21C, which is the image reproduced on the retina after passing through the phase-masks and the eye model. The image distortion is clearly observed without our corrective phase-mask.

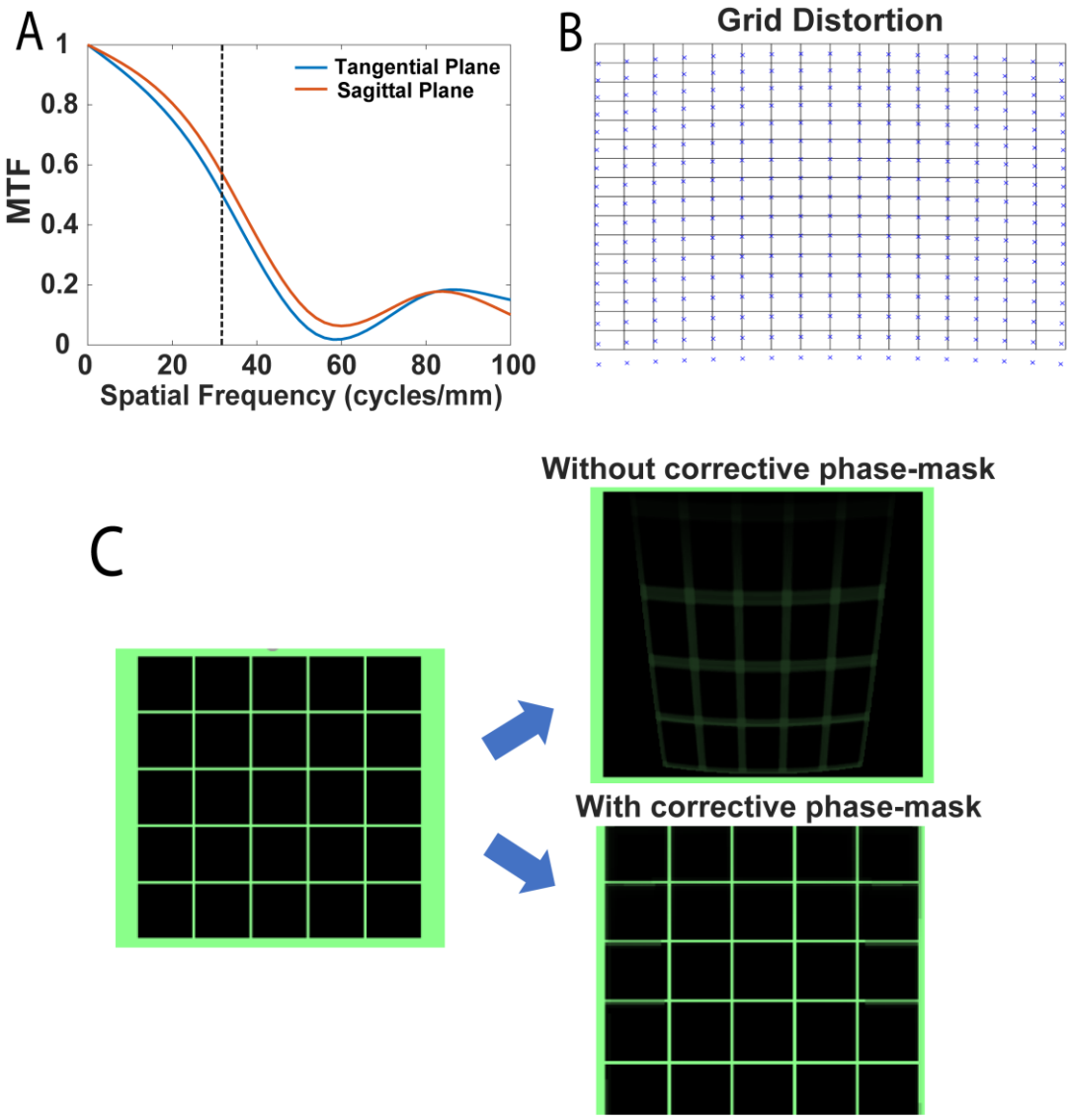

Figure 21. (A) MTF of the NEV calculated in ZEMAX on tangential and sagittal plane. (B) Grid distortion of the NEV corresponds to 10mm × 10mm display size. Highest calculated distortion is 5.9% at the corners. The corresponding operation wavelength here is 540 nm. (C) Image simulation of the green cross bars passing through NEV using Zemax. The left figure is the original image that is seen in real world. The right figure is the simulated image as seen by the person using NEV before and after adding corrective phase-mask.

So far, we assumed the NEV to be made of bilayer, ideal phase masks. In practice, these masks will be implemented using metasurfaces. The proposed stack of metasurfaces is shown in Fig. 22A. The partially reflective metasurface is designed by placing silicon nitride nano-scatterers on a partially reflective distributed Bragg reflector (DBR) with two layers of silicon nitride and two layers of silicon oxide [104]. The resulting phase and amplitude of the reflected light as a function of pillar diameter (duty cycle) are shown in Fig. 22B. Note that the amplitude of the reflected light is ~30%, whereas the phase covers the full 0-2π range. Engineering high reflective silicon nitride metasurfaces without DBR is not trivial (due to the low refractive index of SiN) over the whole 0-2π phase range and using DBR layers helps us to increase this reflection efficiency up to 30% for the first metasurface while maintaining the full 0-2π phase range. The second metasurface will be a transmissive one, whose transmission parameters are shown in Fig. 22C. The sharp resonances observed in the phase and amplitude correspond to guided mode resonances and are excluded when designing the final metasurface by selecting pillar diameters off resonance. The design process involves selecting the appropriate spatial phase profile for the specific optical component, arranging the scatterers on a subwavelength lattice, and spatially varying their dimensions. Inset figure of Fig. 22B. and 22C. shows cylindrical post formation including their substrates. The DBR structure in Fig. 22B. is designed for 540 nm wavelength so their thickness is 67.5 nm for SiN and 90 nm for oxide. The metasurface periodicity *p* and thickness *t* for both metasurfaces here are set to 443 nm and 700 nm respectively. The periodicity and thickness are chosen to maximize the transmission efficiency for second metasurface while maintaining the full 0-2π phase coverage. All the simulations that we have done so far were for normal incident angle as shown in Fig. 22. However, based on our design schematic and display position in Fig. 20., our reflective metasurface will experience an angle of incidence from 40° to

50˚. It is necessary for us to get the whole 0-2π phase coverage at these angles as well which is presented in more detail in section 4.5.1 (Fig. 25).

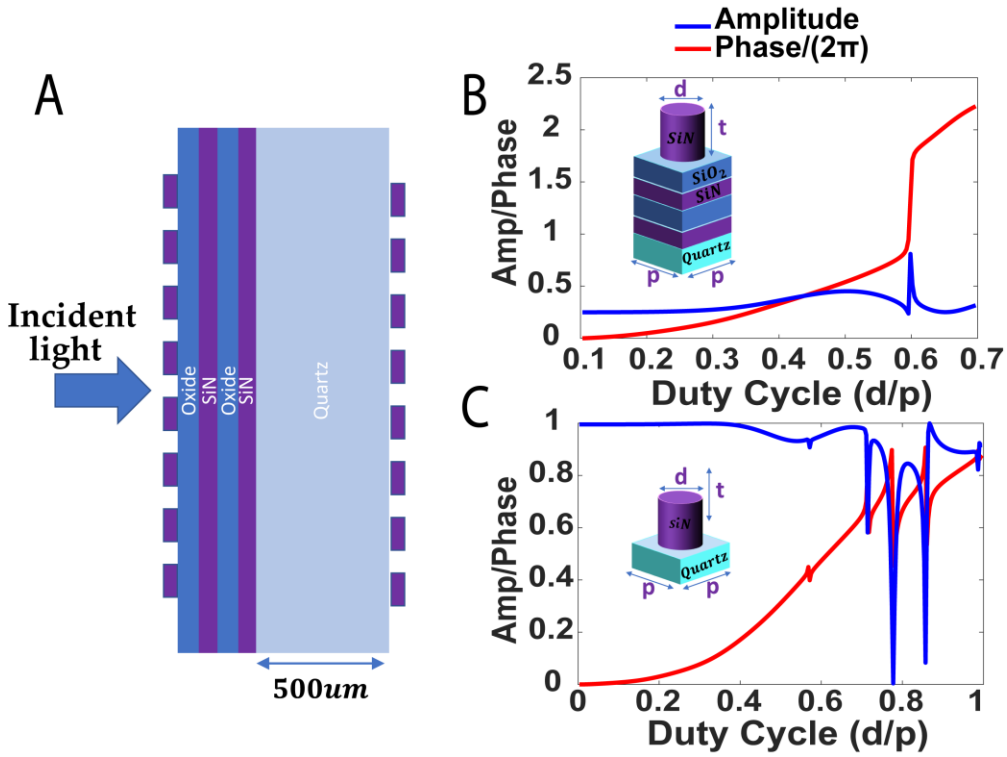

Figure 22. Metasurface (MS) implementation of the phase-masks: (a) schematic of the metasurface stack; the simulate phase and amplitude response of the (B) light reflected from the first metasurface and (C) light transmitted through the second metasurface. These plots are calculated using rigorous coupled wave analysis.

4.3 Multi-wavelength Metasurface

One of the major issues facing metasurfaces is their strong chromatic aberrations. For example, a metalens will produce a focused image at one wavelength and an unfocused image at another [105]. A successful AR visor, however, must produce focused images at multiple wavelengths, specifically red, green, and blue in order to display images for all perceivable colors.

Much work has been done to produce multiwavelength achromatic metalenses (MAM) including multiplexing different functionalities in a single metasurface [106] or dispersion engineering [107], but until recently previous methods either have not been shown to work in the visible spectrum or have limitations on device size and the phase shift that can be imparted. Furthermore, such approaches have worked well for high-contrast scatterers (like silicon scatterers working in the infrared with refractive index n~3.5), as the light remains tightly confined inside the scatterer, and thus the coupling between different scatterers is minimized. Unfortunately, our application at visible wavelengths precludes silicon as the material of choice, and we have to rely on silicon nitride (n~2) and silicon dioxide (n~1.5), both of which are transparent and low index materials relative to silicon. The method described in Ref. [108], however, showed that it is possible to produce a metalens that operates at discrete wavelengths with large differences in the required phase shift at each wavelength. Our metasurface design employs this same method and demonstrates that guided mode resonances (GMR) can give rise to numerous 0-2π phase shift cycles observed for the duty cycle range for pillars using silicon nitride.

Our metasurface visor has a target phase profile at each wavelength that is position dependent. The pillar at any position on the visor must match the desired phases of all three wavelengths (R (700 nm), G (540 nm), B (460nm)) at that position simultaneously. Typically, for a monochromatic metasurface, when the phase shift of a pillar is chosen, the phase that it imparts at other wavelengths is then determined as well. Said another way, for a given phase shift, there is typically only one corresponding pillar size at each wavelength that imparts that phase shift. However, by scatterer design, we can have multiple pillar sizes at each wavelength that impart the desired phase shift. This enables us to better match phase profiles at different wavelengths as we can keep the phase shift at one wavelength fixed while selecting a different pillar size that may

better match the phase profile at another wavelength. This one-to-many relationship between phase and pillar size is achieved by choosing pillar parameters such that the imparted phase shift spans 0-2π multiple times over the range of possible pillar sizes (Fig. 23.). The greater number of 0-2π cycles at each wavelength, the better we can design a metasurface that matches the phase profiles of all wavelengths. This approach is aided by the occurrence of GMR, which cause sudden, abrupt phase shifts that increase the number of pillar sizes available to fulfill a target phase shift.

Using rigorous coupled wave analysis (RCWA) [109], reflection coefficients and phases for pillars ranging in diameter from 10 to 90 percent of the periodicity were calculated for each wavelength. The lattice periodicity *p* and thickness *t* at all wavelengths here are set to 443 nm and 1500 nm, respectively, to achieve multiple 0-2π cycles at all three wavelengths. Pillars with reflection coefficients below 0.3 at any wavelength were removed from consideration as we want to strike a balance between transmission and reflection to maintain a partially reflective visor. For each discretized position in a phase mask, the remaining pillars were assigned an error weight calculated as the square of the difference between the phase mask at that position and the pillar's phase shift at that phase mask's wavelength. The metasurface in our proposed structure was then designed by selecting pillars with the smallest cumulative error (ϵ) across the three phase masks at each position, which is given by:

$$\epsilon(\mathrm{x},\mathrm{y},\mathrm{r}) = \sum_{\mathrm{i}=1}^{\mathrm{n}} \sqrt{\left(\phi(x,y,\lambda_i) - f(r,\lambda_i)\right)^2}$$

Where (x, y) is the position on the phase mask, λ_i is the design wavelength, r is the pillar radius, and n is the number of wavelengths (here $n = 3$). The desired phase is given by ϕ and the calculated phase shift for each pillar is given by f. The final radii distribution of our multi-wavelength reflective metasurface visor is shown in Fig. 23A. We emphasize that, in this method,

we are primarily designing a metasurface that works at certain specific wavelengths, and true broadband operation is not expected. Hence, we need to rely on a display that supports only discrete wavelengths, such as a laser-based display [120].

We then validated our design of a reflective metasurface visor by importing the phase profiles that is provided by our final optimized scatterer distribution into the NEV structure via ray optic simulation which is shown in Fig.20. **Table 5** provides the modulation transfer function (MTF) for three colors at 33 cycles/mm (via Zemax). The MTFs for the multiwavelength metasurface are comparable to that of the monochrome design, exhibiting minimal degradation in performance. This clearly demonstrates that the multi-color metasurface does not degrade the performance of the visor compared to monochromatic metasurface one. We also analyzed the bandwidth of the light-source for the display, and we found that the MTF does not fall very quickly, and at least works for over a ~20 nm bandwidth. We define the bandwidth by the range of wavelengths over which the MTF exceeds 0.3 at 33 cycles/mm (Section 4.5.2). Hence, in some cases, we also can use a narrowband light emitting diodes (LEDs), such as an organic LED, instead of a laser for the display.

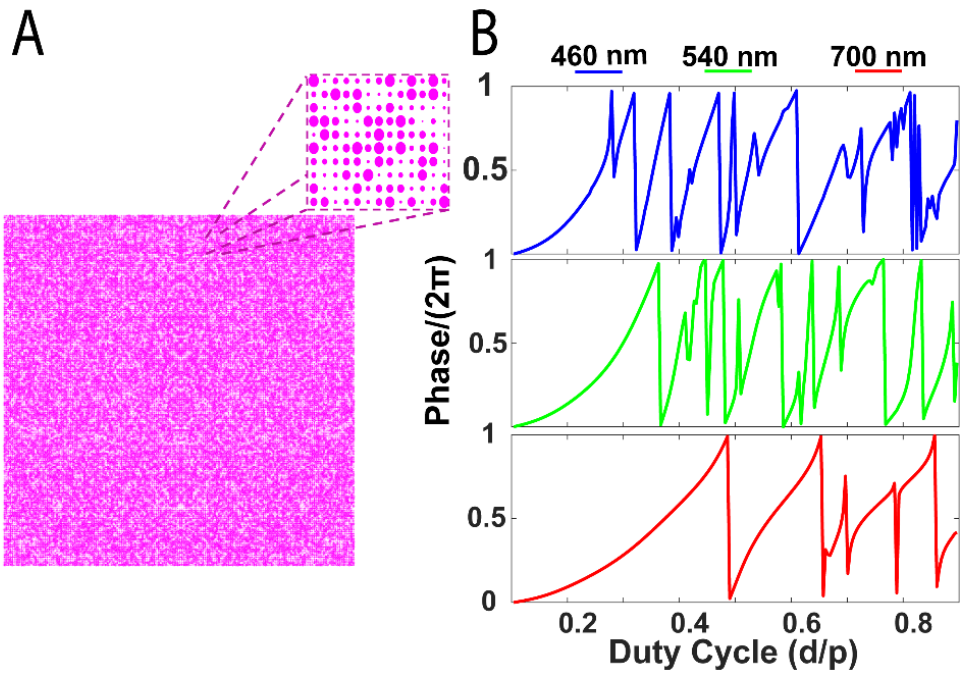

Figure 23. A) Final radii distribution of our multi-wavelength reflective metasurface visor using our optimization method. The diameters of nanopillars are changing from 46 nm to 398 nm. B) Phase of the reflected light through a scatterer using RCWA as a function of duty cycles of nanopillar at wavelengths of 460, 540, and 700 nm. As the pillar width changes, the corresponding phase undergoes multiple 0-2π phase cycles. The sharp phase jumps reflect the excitation of guided mode resonance (GMR).

Table 5. AR visor performance in terms of MTF before and after RGB optimization

Wavelength (nm)	**460**	**540**	**700**
Single wavelength metasurface visor (cycles/mm)	**0.61**	**0.49**	**0.53**
multi-wavelength metasurface visor (cycles/mm)	**0.51**	**0.47**	**0.49**

Once we finalize the multi-wavelength reflective visor design, we then optimize the design for the second metasurface at the central wavelength. We found that while the second metasurface is designed to negate the effect of the first metasurface, such negation happens over the full wavelength range simulated. As can be seen in Fig. 24, the RMS wavefront error is minimal over a broad optical bandwidth (simulated for different angles).

Additionally, we simulate an image of the white crossbars in Zemax to evaluate the see-through quality, as shown in Fig. 24.B. The projected image of the crossbars is shown in the right side of Fig. 24B, which is the image reproduced on the retina after passing through the metasurface layers and the eye model. We can clearly observe that the rainbow effect caused by chromatic aberration of these metasurfaces are negligible.

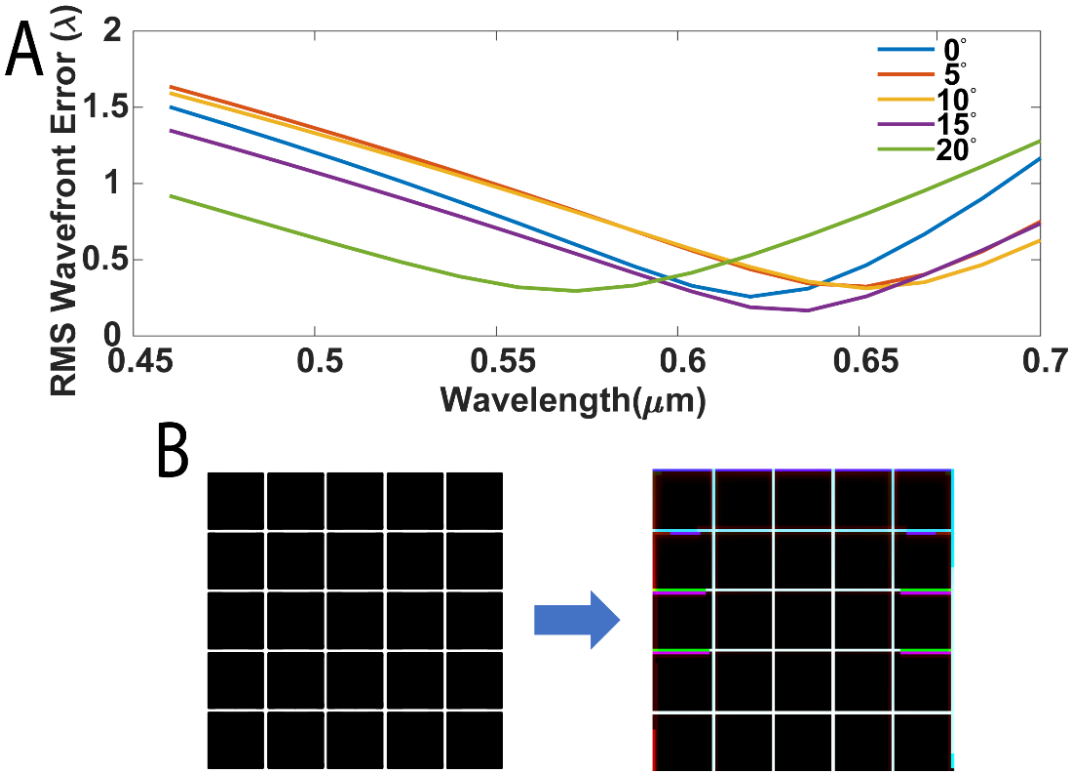

Figure 24. A) RMS wavefront error in visible range calculated for the transmitted light through the visor (light that passes through two metasurfaces) in five different incident angles. B) Image simulation of the white cross bars passing through NEV using Zemax. The left figure is the original image that is seen in real world. The right figure is the simulated image as seen by the person using NEV.

Our work explored the possibility of using a metasurface to design and create a compact near-eye visor which provides a large field of view and also reasonable see-through quality for an immersive AR experience. The proposed metasurface visor does not suffer from chromatic aberrations, while providing a large display field of view (>77° both horizontally and vertically), and good (>70% transmission and no distortion) see-through quality.

The current visor includes two layers of metasurfaces which have different phase masks. The scatterers in the metasurface near the eye (which is reflecting the virtual world to the eye) are

designed to have 30% reflectivity and multi-chrome behavior, whereas the scatterers in the metasurface further from the eye (which helps improve the see-through quality) are designed to have close to 100% transmission. The main idea behind our multi-chrome behavior is that we start with the desired phase profiles for each color, and then find the scatterer distribution that provide the phase profiles closest to the desired one.

In this work, we focused on design and simulation of the whole AR metasurface visor due to the complexity of design. Additionally, there are many other relevant factors for high-quality immersive AR experience including large eye-box, high efficiency, broadband operation and tunability (to mitigate VAC) which are not specified in our current architecture. However, we believe that the demonstrated multi-layer metasurface visor is capable of addressing those issues.

4.4 METASURFACE-BASED AR FABRICATION

In the previous section, we proposed composite metasurface visor that can overcome the bulkiness, FOV limitations, chromatic aberrations, and see-through quality of existing NEVs. Using our proposed structure, we can make the eye-wear devices flat and ultra-thin and close to eye, while maintaining a large FOV for virtual world. However, there are some challenges with the current design, including small eye-box, scattered light from possible back reflection and large area fabrication. The eye-box for our current visor is 2.5mm×2.5mm (denoting exit pupil diameter without any expansion) which is lower than current waveguide-base visors [121], although there are some solutions to increase the eye-box by multiplexing different phase-masks into one metasurface [122]. In addition, there could be some additional noise due to the back reflected light from second metasurface. However, our second metasurface is designed to be fully transmissive

(>98%). To mitigate the impact of this possible < 2% back reflection from the second metasurface in future work, we can apply an antireflection coating incorporated with our scatters or instead employ a modified scatter design to maximize this to > 99 % transmission. A complete stray light analysis is warranted to establish the efficacy of our method for building NEV. A full-wave stray light analysis of the actual NEV, however, is not feasible owing to its large size. Hence, we instead used a combination of RCWA and ray optics simulation in this paper, which together show little effects from the stray light.

Another remaining issue is fabrication. While the fabrication of the current design is challenging, fabrication methods already exist that show that such large-area fabrication using Deep Ultra-Violet (DUV) Lithography is possible with high throughput. We also have simulated the tolerance of the metasurfaces to lateral misalignment in terms of acceptable RMS wavefront error range (Section 4.5.3). Two metasurfaces will be fabricated on opposite sides of a 500-μm-thick quartz substrate. Silicon-nitride film will be deposited on both sides of the substrate using plasma-enhanced chemical vapor deposition (PECVD). One of the challenging tasks will be to align two metasurfaces during fabrication on both side of a quartz substrate. To solve this, we will also create registration alignment marks on both side of the substrate using photolithography and ABM aligner. The reflective metasurface (Metasurface I) pattern will be exposed via electron-beam lithography on one side of the sample. After the lithography step, a layer of aluminum will be evaporated onto the sample. After performing lift-off, the sample will be etched using an inductively coupled plasma etcher, and the remaining aluminum will be removed in photoresist developer. To protect the patterns from mechanical damage during the processing of the other side of the sample, a thick layer of SU-8 polymer will be spin-coated over the nanoposts, yielding a rigid planarized layer that will encapsulate and protect the nanoposts. The corrective metasurface

(Metasurface II) will be fabricated on the other side of the substrate using the same processing steps as used for the fabrication of metasurface I.

4.5 MATERIAL AND METHODS

4.5.1 *Angle dependency*

All the RCWA simulations for the phase and amplitude calculation (in reflection and transmission mode) were performed under normal incidence as shown in Fig.22. However, based on our design schematic and display position in Fig. 20., our reflective metasurface will experience an angle of incidence from 40° to 50°. It is necessary for us to get the whole 0-2π phase coverage at these angles as well. As it is shown in Fig. 25., at these angles we still get multiple wraps of 0-2π phase change which is ideal for our multi-wavelength design approach. Here, the operation wavelength for angle dependency simulation is 540 nm.

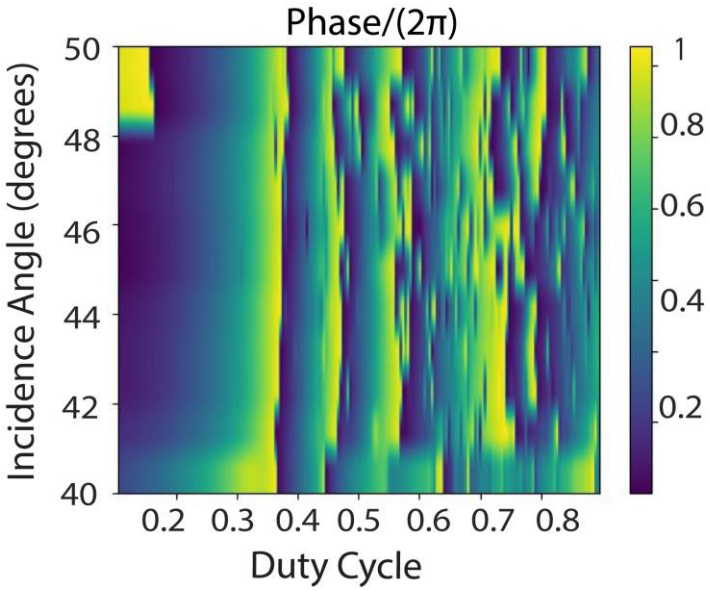

Figure 25. Angle dependency RCWA simulation from 0 to 2π for one wavelength (540 nm). Duty cycle is defined as the ratio of the post diameter to the periodicity. Parameters of pillars are the same for Fig.22.

4.5.2 *Bandwidth Tolerance*

As we mentioned previously in this chapter, we have primarily designed a metasurface that works at certain specific wavelengths, and true broadband operation is not expected here. However, we also analyzed the bandwidth of the light-source for the display, and we found that the MTF does not fall very quickly, and at least works for over a ~20 nm bandwidth. We define the bandwidth by the range of wavelengths over which the MTF exceeds 0.3 at 33 cycles/mm (Fig. 26.). Hence, we can use an LED instead of a laser for the display.

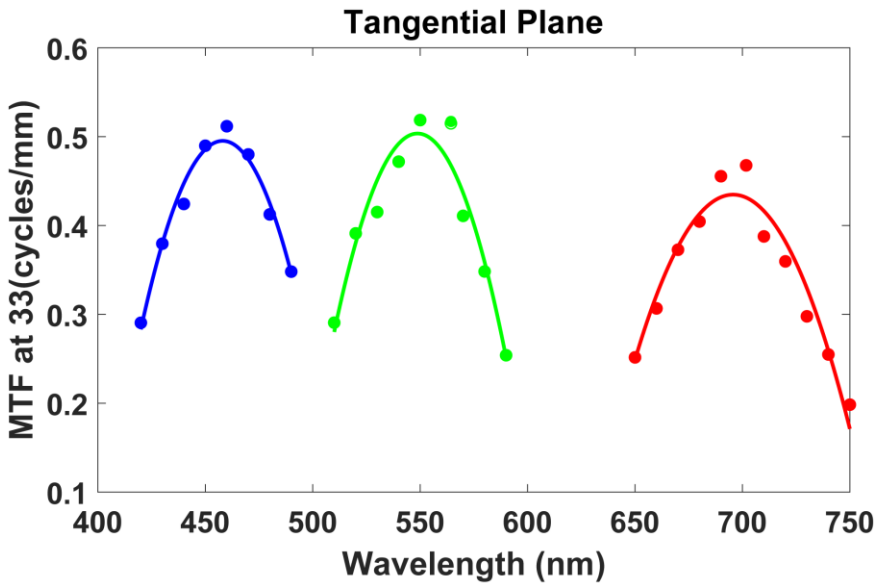

Figure 26. The MTF of the blue, green and red color for the reflective visor at 33 cycles/mm in tangential plane. MTFs above 0.3 at 33 cycle/mm are our evaluation point for acceptable bandwidth.

4.5.3 *Fabrication Tolerance*

While the fabrication of the current design is challenging, fabrication methods already exist that show that such large-area fabrication using DUV Lithography is possible with high throughput. One of the challenging tasks will be to align two metasurfaces during fabrication on both side of a quartz substrate. Here, we have simulated the tolerance of the metasurfaces to lateral misalignment. In this test simulation, the operation wavelength is 540nm and the angle of incidence is assumed to be normal. We are looking for changes in RMS wavefront error in see through mode. We found out that up to 100μm misalignment, error remains below one wavelength, which is still close to our current RMS at normal incident angle.

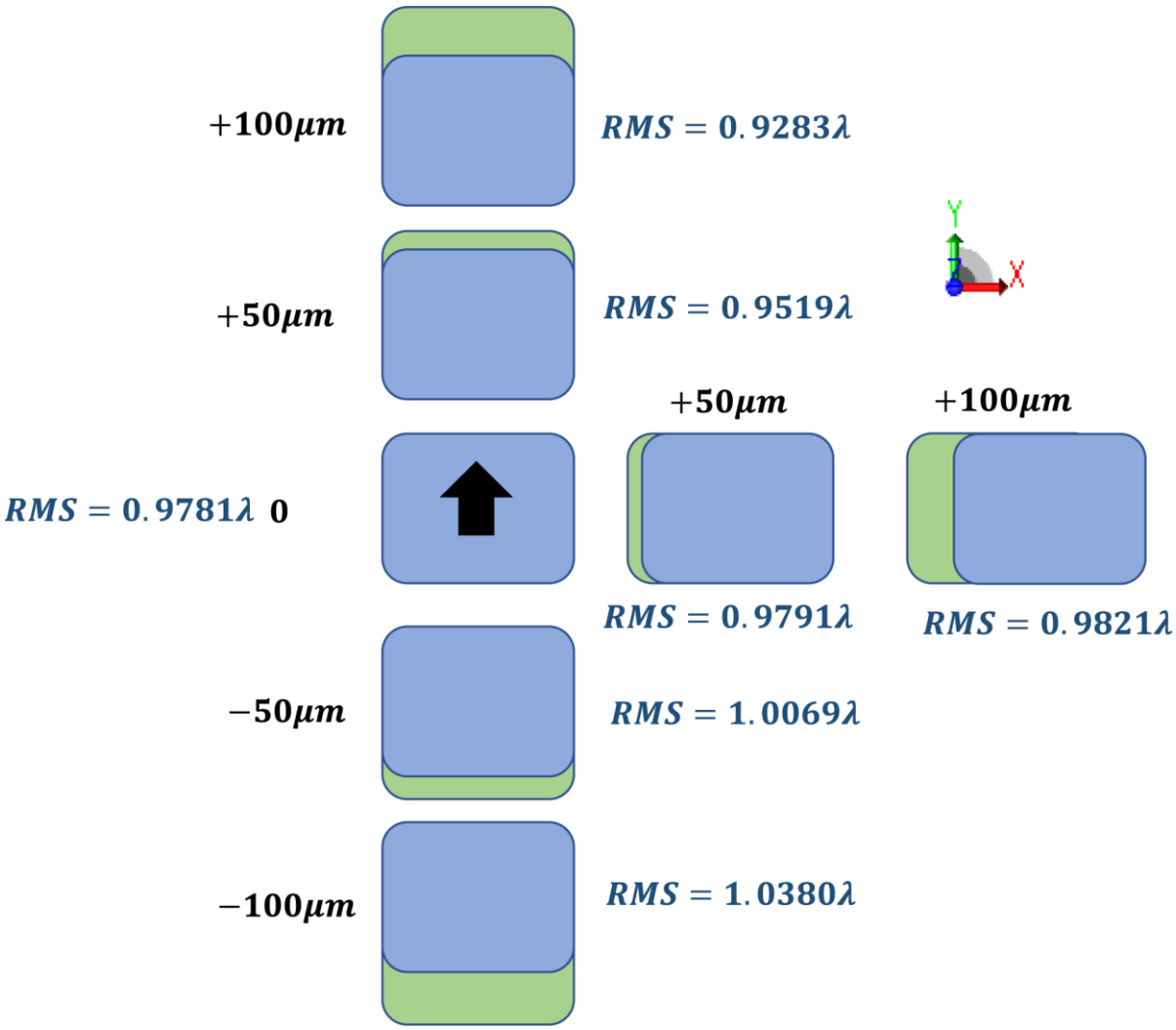

Figure 27. Analysis of lateral tolerance in terms of the RMS wavefront error in the transmitted light. Up to ~100μm misalignment, error remains below one wavelength. The operation wavelength here is 540nm and the angle of incidence is assumed to be normal. The blue box represents the first metasurface (Reflective phase-mask), and the green represents the second metasurface (Corrective phase-mask). The arrow mark shows us which side of the metasurface is up compared to our eye view.

Chapter 5. CONCLUDING REMARKS

In this dissertation, I have explained the motivation for designing metasurfaces, and subsequently detailed what characterizes them. I have also shared the design and fabrication processes, showing how metasurfaces can be built into optical systems for both imaging and non-imaging applications. Based on my individual and collaborative research, I have been able to demonstrate that metasurfaces have great potential to aid in the downscaling of optical elements, particularly in complex optical systems. The potential for downscaling comes from metasurface facilitation of miniaturization and multi-functionality, two characteristics that are significant on their own, and increase in significance due to their interrelated nature. I have also discussed some of the limitations to the metasurface optical systems, and explored some possible solutions to address chromatic aberrations, improve efficiency, and address the occurrence of image quality reductions.

In the body of this dissertation, I investigated how to design dielectric metasurface subwavelength scattering elements to optimize them for a variety of functions. These designs represent the research progress made towards developing optical senses for imaging and non-imaging systems that are more compact. In particular, I presented designs for silicon nitride based scattering elements for 1D and 2D EDOF metasurfaces in the visible regime for full color imaging. I also explained how a more general methodology such using EDOF lenses in conjunction with computational imaging can be applied to eliminate chromatic aberrations at discrete wavelengths. Additionally, I proposed a design for a composite metasurface visors that can overcome several challenges of near eye augmented reality visors, including reduced bulkiness, addressing FOV limitations, reducing chromatic aberrations and improving the see-through quality.

We began this dissertation by evaluating low-loss dielectric materials with a wide range of refractive indices for designing metalenses using both forward and inverse design methodologies. We found reasonable agreement between both methods in terms of the focusing efficiency and the FWHM of the focal spots on the material refractive indices. We found that for low numerical apertures ($NA < 0.6$), the efficiency of the metalenses is almost independent of the refractive index. For higher numerical apertures, however, high-index materials provide higher efficiency. The relationship between refractive index and metalens performance is significant in choosing appropriate material, based on considerations like ease and scalability of manufacturing, or better tunability.

After exploring the limitations of metasurface lenses in terms of material of choices available, we then shifted towards detailing some of our own contributions in the area of full-color imaging with metasurfaces. We demonstrated inverse designed EDOF cylindrical metalenses for the first-time, for various applications in computational imaging and microscopy. We showed that EDOF lenses can alleviate the need for stringent alignment requirements for imaging systems. We then summarized our work on developing a 2D EDOF metalens using inverse design method that has a symmetric PSF, large spectral bandwidth, and that also maintains focusing efficiency comparable to that of a traditional metalens. The proposed inverse designed EDOF meta-optics in conjunction with computational imaging is used to mitigate the chromatic aberrations of traditional metalenses. Unlike other existing EDOF metalenses (log-asphere lenses or other variants), our inverse-designed EDOF metalens represents a highly invariant PSF across a large spectral bandwidth to improve the full-color image quality. We have quantified this via calculating and comparing the PSF correlation coefficient with other EDOF metalenses over the visible spectral

range. We emphasize that this is the largest aperture (1 mm) meta-optics ever reported for achromatic imaging, and as such there is no fundamental limitation on increasing aperture, like dispersion engineered meta-optics do. While we extended the spectral bandwidth and demonstrated achromatic imaging even without post processing algorithms, our images still need to be computationally processed to give us in-focus and better-quality images. This postprocessing adds latency and power to the imaging system. Additionally, we have primarily focused on chromatic aberration corrections, and Seidel aberrations are largely ignored. Using a more involved figure of merit and including the angular dependence, a longer depth of focus metalens can be designed, which can potentially preclude the use of computational postprocessing. In this work, we also emphasized the utility of rotationally symmetric EDOF metalenses (for simplified packaging and mitigating deconvolution artifacts), as well as larger apertures (1 mm) compared to our previous works. A larger aperture will enable more light collection, higher signal-to-noise ratio, and faster shutter speed, which are crucial for practical applications. We envision that the image quality can be further improved by co-designing the meta-optics and computational back end, as has already been reported to provide very high-quality imaging.

Finally, in the previous chapter, we detailed our work on using metasurfaces for a more complex optical system such as Augmented and Virtual Reality visor. we proposed composite metasurface visor that can overcome the bulkiness, FOV limitations, chromatic aberrations, and see-through quality of existing NEVs. Using our proposed structure, we can make the eye-wear devices flat and ultra-thin and close to eye, while maintaining a large FOV for virtual world.

REFERENCES

[1] Yu, Nanfang, and Federico Capasso. "Flat optics with designer metasurfaces." Nature materials 13, no. 2 (2014): 139.

[2] Vo, Sonny, David Fattal, Wayne V. Sorin, Zhen Peng, Tho Tran, Marco Fiorentino, and Raymond G. Beausoleil. "Sub-wavelength grating lenses with a twist." IEEE Photonics Technology Letters 26, no. 13 (2014): 1375-1378.

[3] Arbabi, Amir, Yu Horie, Alexander J. Ball, Mahmood Bagheri, and Andrei Faraon. "Subwavelength-thick lenses with high numerical apertures and large efficiency based on high-contrast transmitarrays." Nature communications 6 (2015): 7069.

[4] Fattal, David, Jingjing Li, Zhen Peng, Marco Fiorentino, and Raymond G. Beausoleil. "Flat dielectric grating reflectors with focusing abilities." Nature Photonics 4, no. 7 (2010): 466.

[5] Yang, Yuanmu, Wenyi Wang, Parikshit Moitra, Ivan I. Kravchenko, Dayrl P. Briggs, and Jason Valentine. "Dielectric meta-reflectarray for broadband linear polarization conversion and optical vortex generation." Nano letters 14, no. 3 (2014): 1394-1399.

[6] Li, Guixin, Ming Kang, Shumei Chen, Shuang Zhang, Edwin Yue-Bun Pun, Kok Wai Cheah, and Jensen Li. "Spin-enabled plasmonic metasurfaces for manipulating orbital angular momentum of light." Nano letters 13, no. 9 (2013): 4148-4151.

[7] Zheng, Guoxing, Holger Mühlenbernd, Mitchell Kenney, Guixin Li, Thomas Zentgraf, and Shuang Zhang. "Metasurface holograms reaching 80% efficiency." Nature nanotechnology 10, no. 4 (2015): 308.

[8] Ni, Xingjie, Alexander V. Kildishev, and Vladimir M. Shalaev. "Metasurface holograms for visible light." Nature communications 4 (2013): 2807.

[9] Yu, Nanfang, Francesco Aieta, Patrice Genevet, Mikhail A. Kats, Zeno Gaburro, and Federico Capasso. "A broadband, background-free quarter-wave plate based on plasmonic metasurfaces." Nano letters 12, no. 12 (2012): 6328-6333.

[10] Arbabi, Amir, Yu Horie, Mahmood Bagheri, and Andrei Faraon. "Dielectric metasurfaces for complete control of phase and polarization with subwavelength spatial resolution and high transmission." Nature nanotechnology 10, no. 11 (2015): 937.

[11] Zhan, A., Colburn, S., Dodson, C.M. and Majumdar, A., 2017. Metasurface freeform nanophotonics. *Scientific reports, 7*(1), p.1673.

[12] Fattal, David, Jingjing Li, Zhen Peng, Marco Fiorentino, and Raymond G. Beausoleil. "Flat dielectric grating reflectors with focusing abilities." Nature Photonics 4, no. 7 (2010): 466.

[13] Khorasaninejad, Mohammadreza, Wei Ting Chen, Alexander Y. Zhu, Jaewon Oh, Robert C. Devlin, Charles Roques-Carmes, Ishan Mishra, and Federico Capasso. "Visible wavelength planar metalenses based on titanium dioxide." IEEE Journal of Selected Topics in Quantum Electronics 23, no. 3 (2017): 43-58.

[14] Wang, Zhenhai, Shumin He, Qifa Liu, and Wei Wang. "Visible light metasurfaces based on gallium nitride high contrast gratings." Optics Communications 367 (2016): 144-148.

[15] Zhan, Alan, Shane Colburn, Rahul Trivedi, Taylor K. Fryett, Christopher M. Dodson, and Arka Majumdar. "Low-contrast dielectric metasurface optics." ACS Photonics 3, no. 2 (2016): 209-214.

[16] Colburn, Shane, Alan Zhan, Elyas Bayati, James Whitehead, Albert Ryou, Luocheng Huang, and Arka Majumdar. "Broadband transparent and CMOS-compatible flat optics with silicon nitride metasurfaces." Optical Materials Express 8, no. 8 (2018): 2330-2344.

[17] Reddy, R. R., and Y. Nazeer Ahammed. "A study on the Moss relation." Infrared physics & technology 36, no. 5 (1995): 825-830.

[18] Yang, J. and J.A. Fan, Analysis of material selection on dielectric metasurface performance. Optics express, 2017. 25(20): 23899-23909.

[19] Lalanne, Philippe, and Pierre Chavel. "Metalenses at visible wavelengths: past, present, perspectives." *Laser & Photonics Reviews* 11.3 (2017): 1600295.

[20] H. Liang, Q. Lin, X. Xie, Q. Sun, Y. Wang, L. Zhou, L. Liu, X. Yu, J. Zhou, T. F. Krauss, J. Li, Nano Lett.2018, 18, 4460

[21] Paniagua-Dominguez, Ramon, et al. "A metalens with a near-unity numerical aperture." *Nano letters* 18.3 (2018): 2124-2132.

[22] Jenkins, Francis A., and Harvey E. White. Fundamentals of optics. Tata McGraw-Hill Education, 1937.

[23] Chen, F. T., and H. G. Craighead. "Diffractive phase elements based on two-dimensional artificial dielectrics." Optics letters 20, no. 2 (1995): 121-123.

[24] Søndergaard, Roar, Markus Hösel, Dechan Angmo, Thue T. Larsen-Olsen, and Frederik C. Krebs. "Roll-to-roll fabrication of polymer solar cells." Materials today 15, no. 1-2 (2012): 36-49.

[25] Chen, Frederick T., and Harold G. Craighead. "Diffractive lens fabricated with mostly zeroth-order gratings." Optics letters 21, no. 3 (1996): 177-179.

[26] Liu, Victor, and Shanhui Fan. "S4: A free electromagnetic solver for layered periodic structures." Computer Physics Communications 183, no. 10 (2012): 2233-2244.

[27] Zhan, Alan, Taylor K. Fryett, Shane Colburn, and Arka Majumdar. "Inverse design of optical elements based on arrays of dielectric spheres." Applied optics 57, no. 6 (2018): 1437-1446.

[28] Stork, Wilhelm, Norbert Streibl, H. Haidner, and P. Kipfer. "Artificial distributed-index media fabricated by zero-order gratings." Optics letters 16, no. 24 (1991): 1921-1923.

[29] Rosenblatt, David, Avener Sharon, and Asher A. Friesem. "Resonant grating waveguide structures." IEEE Journal of Quantum electronics 33, no. 11 (1997): 2038-2059.

[30] Sell, David, Jianji Yang, Sage Doshay, Rui Yang, and Jonathan A. Fan. "Large-angle, multifunctional metagratings based on freeform multimode geometries." Nano letters 17, no. 6 (2017): 3752-3757.

[31] Wang, Ke, Jie Zhao, Qiang Cheng, and Tie Jun Cui. "Broadband and broad-angle low-scattering metasurface based on hybrid optimization algorithm." Scientific reports 4 (2014): 5935.

[32] Aieta, Francesco, Mikhail A. Kats, Patrice Genevet, and Federico Capasso. "Multiwavelength achromatic metasurfaces by dispersive phase compensation." Science 347, no. 6228 (2015): 1342-1345.

[33] Pestourie, Raphaël, Carlos Pérez-Arancibia, Zin Lin, Wonseok Shin, Federico Capasso, and Steven G. Johnson. "Inverse design of large-area metasurfaces." Optics Express 26, no. 26 (2018): 33732-33747.

[34] Mackowski, Daniel W., and Michael I. Mishchenko. "Calculation of the T matrix and the scattering matrix for ensembles of spheres." JOSA A 13, no. 11 (1996): 2266-2278.

[35] Egel, Amos, Lorenzo Pattelli, Giacomo Mazzamuto, Diederik S. Wiersma, and Uli Lemmer. "CELES: CUDA-accelerated simulation of electromagnetic scattering by large ensembles of spheres." Journal of Quantitative Spectroscopy and Radiative Transfer 199 (2017): 103-110.

[36] Maznev, A. A., and O. B. Wright. "Upholding the diffraction limit in the focusing of light and sound." Wave Motion 68 (2017): 182-189.

[37] Yang, Jianji, David Sell, and Jonathan A. Fan. "Freeform metagratings based on complex light scattering dynamics for extreme, high efficiency beam steering." Annalen der Physik 530, no. 1 (2018): 1700302.

[38] Sell, D., Yang, J., Doshay, S., Yang, R., & Fan, J. A. (2017). Large-angle, multifunctional metagratings based on freeform multimode geometries. *Nano letters*, *17*(6), 3752-3757.

[39] Schmitt, N., Georg, N., Brière, G., Loukrezis, D., Héron, S., Lanteri, S., ... & Vézian, S. (2019). Optimization and uncertainty quantification of gradient index metasurfaces. *Optical Materials Express*, *9*(2), 892-910.

[40] Zhan, A., Fryett, T. K., Colburn, S., & Majumdar, A. (2018). Inverse design of optical elements based on arrays of dielectric spheres. *Applied optics*, *57*(6), 1437-1446.

[41] Callewaert, F., Butun, S., Li, Z., & Aydin, K. (2016). Inverse design of an ultra-compact broadband optical diode based on asymmetric spatial mode conversion. *Scientific reports*, *6*(1), 1-10.

[42] Zhan, A., Gibson, R., Whitehead, J., Smith, E., Hendrickson, J. R., & Majumdar, A. (2019). Controlling three-dimensional optical fields via inverse Mie scattering. *Science advances*, *5*(10), eaax4769.

[43] Lin, Z., Groever, B., Capasso, F., Rodriguez, A. W., & Lončar, M. (2018). Topology-optimized multilayered metaoptics. *Physical Review Applied*, *9*(4), 044030.

[44] Lin, Z., Liu, V., Pestourie, R., & Johnson, S. G. (2019). Topology optimization of freeform large-area metasurfaces. *Optics express*, *27*(11), 15765-15775.

[45] Chung, H., & Miller, O. D. (2020). High-NA achromatic metalenses by inverse design. *Optics Express*, *28*(5), 6945-6965.

[46] Phan, T., Sell, D., Wang, E. W., Doshay, S., Edee, K., Yang, J., & Fan, J. A. (2019). High-efficiency, large-area, topology-optimized metasurfaces. *Light: Science & Applications*, *8*(1), 1-9.

[47] Shain, W. J., Vickers, N. A., Goldberg, B. B., Bifano, T., & Mertz, J. (2017). Extended depth-of-field microscopy with a high-speed deformable mirror. *Optics letters*, *42*(5), 995-998.

[48] Bradburn, S., Cathey, W. T., & Dowski, E. R. (1997). Realizations of focus invariance in optical–digital systems with wave-front coding. *Applied optics*, *36*(35), 9157-9166.

[49] Colburn, S., Zhan, A., & Majumdar, A. (2018). Metasurface optics for full-color computational imaging. *Science advances*, *4*(2), eaar2114.

[50] Colburn, S., & Majumdar, A. (2019). Simultaneous Achromatic and Varifocal Imaging with Quartic Metasurfaces in the Visible. *ACS Photonics*. *7* (1), 120-127. DOI: 10.1021/acsphotonics.9b01216

[51] George, N., & Chi, W. (2003). Extended depth of field using a logarithmic asphere. *Journal of Optics A: Pure and Applied Optics*, *5*(5), S157.

[52] Feng, D., Ou, P., Feng, L. S., Hu, S. L., & Zhang, C. X. (2008). Binary sub-wavelength diffractive lenses with long focal depth and high transverse resolution. Optics express, 16(25), 20968-20973.

[53] Dong, B. Z., Liu, J., Gu, B. Y., Yang, G. Z., & Wang, J. (2001). Rigorous electromagnetic analysis of a microcylindrical axilens with long focal depth and high transverse resolution. *JOSA A*, *18*(7), 1465-1470.

[54] Mei, G. A., Ye, J. S., Zhang, Y., & Lin, J. (2011). Metallic cylindrical focusing micromirrors with long axial focal depth or increased lateral resolution. *JOSA A*, *28*(6), 1051-1057.

[55] Ye, J. S., Dong, B. Z., Gu, B. Y., Yang, G. Z., & Liu, S. T. (2002). Analysis of a closed-boundary axilens with long focal depth and high transverse resolution based on rigorous electromagnetic theory. *JOSA A*, *19*(10), 2030-2035.

[56] Pestourie, R., Pérez-Arancibia, C., Lin, Z., Shin, W., Capasso, F., & Johnson, S. G. (2018). Inverse design of large-area metasurfaces. *Optics express*, *26*(26), 33732-33747.

[57] E. Arbabi, A. Arbabi, S. M. Kamali, Y. Horie, and A. Faraon, "Multiwavelength polarization-insensitive lenses based on dielectric metasurfaces with meta-molecules," Optica 3, 628–633 (2016).

[58] M. Born, and E. Wolf, Principles of optics: electromagnetic theory of propagation, interference and diffraction of light, 7th (Cambridge University Press, Cambridge, 1999).

[59] Aieta F, Kats MA, Genevet P, Capasso F. Multiwavelength achromatic metasurfaces by dispersive phase compensation. Science 347, 1342–1345 (2015).

[60] Avayu O, Almeida E, Prior P, Ellenbogen T. Composite functional metasurfaces for multispectral achromatic optics. Nat Commun 8, 14992 (2017).

[61] Chen WT, Zhu AY, Sanjeev V, Khorasaninejad M, Shi ZJ et al. A broadband achromatic metalens for focusing and imaging in the visible. Nat Nanotechnol 13, 220–226 (2018).

[62] Wang SM, Wu PC, Su VC, Lai YC, Chen MK et al. A broadband achromatic metalens in the visible. Nat Nanotechnol 13, 227–232 (2018).

[63] M. Khorasaninejad, Z. Shi, A. Y. Zhu, W. T. Chen, V. Sanjeev, A. Zaidi, and F. Capasso, "Achromatic metalens over 60 nm bandwidth in the visible and metalens with reverse chromatic dispersion," Nano Lett. 17, 1819–1824 (2017).

[64] W. T. Chen, A. Y. Zhu, J. Sisler, Z. Bharwani, and F. Capasso, "A broadband achromatic polarization-insensitive metalens consisting of anisotropic nanostructures," Nat. Commun. 10, 355 (2019).

[65] E. Arbabi, A. Arbabi, S. M. Kamali, Y. Horie, and A. Faraon, "Controlling the sign of chromatic dispersion in diffractive optics with dielectric metasurfaces," Optica 4, 625–632 (2017).

[66] W. T. Chen, A. Y. Zhu, F. Capasso, Flat optics with dispersion-engineered metasurfaces. Nat. Rev. Mater. 5, 604–620 (2020).

[67] Presutti, F., & Monticone, F. (2020). Focusing on bandwidth: achromatic metalens limits. Optica, 7(6), 624-631.

[68] Park, J. S., Zhang, S., She, A., Chen, W. T., Lin, P., Yousef, K. M., ... & Capasso, F. (2019). All-glass, large metalens at visible wavelength using deep-ultraviolet projection lithography. Nano letters, 19(12), 8673-8682.

[69] J. N. Mait, G. W. Euliss, and R. A. Athale, "Computational imaging," Adv. Opt. Photonics 10, 409–483 (2018).

[70] S. Colburn and A. Majumdar, "Simultaneous achromatic and varifocal imaging with quartic metasurfaces in the visible," ACS Photonics 7, 120–127 (2019).

[71] L. Ledesma-Carrillo, C. M. Gómez-Sarabia, M. Torres-Cisneros, R. Guzmán-Cabrera, C. Guzmán-Cano, and J. Ojeda-Castañeda, "Hadamard circular masks: high focal depth with high throughput," Opt. Express 25, 17004–17020 (2017).

[72] J. Ojeda-Castaneda, J. E. A. Landgrave, and H. M. Escamilla, "Annular phase-only mask for high focal depth," Opt. Lett. 30, 1647–1649 (2005).

[73] Huang, L., Whitehead, J., Colburn, S., & Majumdar, A. (2020). Design and analysis of extended depth of focus metalenses for achromatic computational imaging. Photonics Research, 8(10), 1613-1623.

[74] George, N., & Chi, W. (2003). Extended depth of field using a logarithmic asphere. Journal of Optics A: Pure and Applied Optics, 5(5), S157.

[75] Sell, D., Yang, J., Doshay, S., Yang, R., & Fan, J. A. (2017). Large-angle, multifunctional metagratings based on freeform multimode geometries. Nano letters, 17(6), 3752-3757.

[76] Schmitt, N., Georg, N., Brière, G., Loukrezis, D., Héron, S., Lanteri, S., ... & Vézian, S. (2019). Optimization and uncertainty quantification of gradient index metasurfaces. Optical Materials Express, 9(2), 892-910.

[77] Zhan, A., Fryett, T. K., Colburn, S., & Majumdar, A. (2018). Inverse design of optical elements based on arrays of dielectric spheres. Applied optics, 57(6), 1437-1446.

[78] Callewaert, F., Butun, S., Li, Z., & Aydin, K. (2016). Inverse design of an ultra-compact broadband optical diode based on asymmetric spatial mode conversion. Scientific reports, 6(1), 1-10.

[79] Zhan, A., Gibson, R., Whitehead, J., Smith, E., Hendrickson, J. R., & Majumdar, A. (2019). Controlling three-dimensional optical fields via inverse Mie scattering. Science advances, 5(10), eaax4769.

[80] Lin, Z., Groever, B., Capasso, F., Rodriguez, A. W., & Lončar, M. (2018). Topology-optimized multilayered metaoptics. Physical Review Applied, 9(4), 044030.

[81] Lin, Z., Liu, V., Pestourie, R., & Johnson, S. G. (2019). Topology optimization of freeform large-area metasurfaces. Optics express, 27(11), 15765-15775.

[82] Chung, H., & Miller, O. D. (2020). High-NA achromatic metalenses by inverse design. Optics Express, 28(5), 6945-6965.

[83] Pestourie, R., Pérez-Arancibia, C., Lin, Z., Shin, W., Capasso, F., & Johnson, S. G. (2018). Inverse design of large-area metasurfaces. Optics Express, 26(26), 33732-33747.

[84] Lin, Z., Roques-Carmes, C., Pestourie, R., Soljačić, M., Majumdar, A., & Johnson, S. G. (2021). End-to-end nanophotonic inverse design for imaging and polarimetry. Nanophotonics, 10(3), 1177-1187.

[85] Li, Z., Pestourie, R., Park, J. S., Huang, Y. W., Johnson, S. G., & Capasso, F. (2021). Inverse design enables large-scale high-performance meta-optics reshaping virtual reality. arXiv preprint arXiv:2104.09702.

[86] Pestourie, R. Assume Your Neighbor is Your Equal: Inverse Design in Nanophotonics. Ph.D. thesis, Harvard University (2020).

[87] Pérez-Arancibia, C., Pestourie, R., & Johnson, S. G. (2018). Sideways adiabaticity: beyond ray optics for slowly varying metasurfaces. Optics Express, 26(23), 30202-30230.

[88] Boyd, J. P. (2001). Chebyshev and Fourier spectral methods. Courier Corporation.

[89] Pestourie, R., Mroueh, Y., Nguyen, T. V., Das, P., & Johnson, S. G. (2020). Active learning of deep surrogates for PDEs: Application to metasurface design. npj Computational Materials, 6(1), 1-7.

[90] Lohmann, A. W. (1989). Scaling laws for lens systems. Applied optics, 28(23), 4996-4998.

[91] F. Presutti and F. Monticone, "Focusing on bandwidth: achromatic metalens limits," Optica 7, 624–631 (2020)

[92] N. Nacereddine, S. Tabbone, and D. Ziou, "Similarity transformation parameters recovery based on Radon transform. Application in image registration and object recognition," Pattern Recogn. 48, 2227–2240 (2015).

[93] Getreuer, P. (2010). tvreg: Variational imaging methods for denoising, deconvolution, inpainting, and segmentation. UCLA Department of Mathematics.

[94] Tseng, E., Colburn, S., Whitehead, J., Huang, L., Baek, S. H., Majumdar, A., & Heide, F. (2021). Neural Nano-Optics for High-quality Thin Lens Imaging. arXiv preprint arXiv:2102.11579.

[95] Lin, Z., Roques-Carmes, C., Pestourie, R., Soljačić, M., Majumdar, A., & Johnson, S. G. (2021). End-to-end nanophotonic inverse design for imaging and polarimetry. Nanophotonics, 10(3), 1177-1187.

[96] Azuma, R., Baillot, Y., Behringer, R., Feiner, S., Julier, S., & MacIntyre, B. (2001). Recent advances in augmented reality. IEEE computer graphics and applications, 21(6), 34-47.

[97] Hu, X., & Hua, H. (2014). High-resolution optical see-through multi-focal-plane head-mounted display using freeform optics. Optics express, 22(11), 13896-13903.

[98] Pan, J. W., Che-Wen, C., Huang, K. D., & Wu, C. Y. (2014). Demonstration of a broad band spectral head-mounted display with freeform mirrors. Optics express, 22(11), 12785-12798.

[99] Yang, J., Twardowski, P., Gérard, P., & Fontaine, J. (2016). Design of a large field-of-view see-through near to eye display with two geometrical waveguides. Optics letters, 41(23), 5426-5429.

[100] Liu, Z., Pan, C., Pang, Y., & Huang, Z. (2019). A full-color near-eye augmented reality display using a tilted waveguide and diffraction gratings. Optics Communications, 431, 45-50.

[101] Yoshida, T., Tokuyama, K., Takai, Y., Tsukuda, D., Kaneko, T., Suzuki, N., ... & Machida, A. (2018). A plastic holographic waveguide combiner for light-weight and highly-transparent augmented reality glasses. Journal of the Society for Information Display, 26(5), 280-286.

[102] Kress, B. C. (2019, July). Optical waveguide combiners for AR headsets: features and limitations. In Digital Optical Technologies 2019 (Vol. 11062, p. 110620J). International Society for Optics and Photonics.

[103] Waldern, J. D., Grant, A. J., & Popovich, M. M. (2018, May). DigiLens switchable Bragg grating waveguide optics for augmented reality applications. In Digital Optics for Immersive Displays (Vol. 10676, p. 106760G). International Society for Optics and Photonics.

[104] Stork, W., Streibl, N., Haidner, H., & Kipfer, P. (1991). Artificial distributed-index media fabricated by zero-order gratings. Optics letters, 16(24), 1921-1923.

[105] Hong, C., Colburn, S., & Majumdar, A. (2017). Flat metaform near-eye visor. Applied Optics, 56(31), 8822-8827.

[106] Lee, G. Y., Hong, J. Y., Hwang, S., Moon, S., Kang, H., Jeon, S., ... & Lee, B. (2018). Metasurface eyepiece for augmented reality. Nature communications, 9(1), 1-10.

[107] Lan, S., Zhang, X., Taghinejad, M., Rodrigues, S., Lee, K. T., Liu, Z., & Cai, W. (2019). Metasurfaces for near-eye augmented reality. ACS Photonics, 6(4), 864-870.

[108] Moon, S., Lee, C. K., Nam, S. W., Jang, C., Lee, G. Y., Seo, W., ... & Lee, B. (2019). Augmented reality near-eye display using Pancharatnam-Berry phase lenses. Scientific reports, 9(1), 1-10.

[109] Kamali, S. M., Arbabi, E., & Faraon, A. (2019, February). Metasurface-based compact light engine for AR headsets. In Optical Design Challenge 2019 (Vol. 11040, p. 1104002). International Society for Optics and Photonics.

[110] Atchison, D. A., & Smith, G. (2000). Optics of the human eye. Butterworth-Heinemann.

[111] Von F, Z. (1934). Beugungstheorie des schneidenver-fahrens und seiner verbesserten form, der phasenkontrastmethode. physica, 1(7-12), 689-704.

[112] Shannon, R. R. (1995). Optical Specification. Handbook of Optics, 1, 35-1.

[113] Cheng, D., Hua, H., & Wang, Y. (2012). U.S. Patent Application No. 13/318,864.

[114] Sheppard, C. J. R. (1995). Approximate calculation of the reflection coefficient from a stratified medium. Pure and Applied Optics: Journal of the European Optical Society Part A, 4(5), 665.

[115] Colburn, S., Zhan, A., & Majumdar, A. (2018). Metasurface optics for full-color computational imaging. Science advances, 4(2), eaar2114.

[116] Arbabi, E., Arbabi, A., Kamali, S. M., Horie, Y., & Faraon, A. (2016). Multiwavelength metasurfaces through spatial multiplexing. Scientific reports, 6, 32803.

[117] Chen, W. T., Zhu, A. Y., & Capasso, F. (2020). Flat optics with dispersion-engineered metasurfaces. Nature Reviews Materials, 1-17.

[118] Shi, Z., Khorasaninejad, M., Huang, Y. W., Roques-Carmes, C., Zhu, A. Y., Chen, W. T., ... & Devlin, R. C. (2018). Single-layer metasurface with controllable multiwavelength functions. Nano letters, 18(4), 2420-2427.

[119] Liu, V., & Fan, S. (2012). S4: A free electromagnetic solver for layered periodic structures. Computer Physics Communications, 183(10), 2233-2244.

[120] Chellappan, K. V., Erden, E., & Urey, H. (2010). Laser-based displays: a review. Applied optics, 49(25), F79-F98.

[121] Miller, J. M., De Beaucoudrey, N., Chavel, P., Turunen, J., & Cambril, E. (1997). Design and fabrication of binary slanted surface-relief gratings for a planar optical interconnection. Applied optics, 36(23), 5717-5727.

[122] Kim, S. B., & Park, J. H. (2018). Optical see-through Maxwellian near-to-eye display with an enlarged eyebox. Optics letters, 43(4), 767-770.

[123] Bayati, E., Zhan, A., Colburn, S., Zhelyeznyakov, M. V., & Majumdar, A. (2019). Role of refractive index in metalens performance. Applied Optics, 58(6), 1460-1466.

[124] Bayati, E., Pestourie, R., Colburn, S., Lin, Z., Johnson, S. G., & Majumdar, A. (2020). Inverse designed metalenses with extended depth of focus. ACS photonics, 7(4), 873-878. Copyright 2020.

[125] Bayati, E., Pestourie, R., Colburn, S., Lin, Z., Johnson, S. G., & Majumdar, A. (2021). Inverse designed extended depth of focus meta-optics for broadband imaging in the visible. Nanophotonics.